DESIGN OF PHOTONIC PHASED ARRAY SWITCHES USING NANO ELECTROMECHANICAL SYSTEMS ON SILICON-ON-INSULATOR INTEGRATION PLATFORM

By
Ali Abdulsattar Hussein

Photonics Technology Laboratory
Center for Research in Photonics at the University of Ottawa
Ottawa, Canada K1N6N5

A thesis submitted to the
Faculty of Graduate and Postdoctoral Studies
in partial fulfillment of the requirements for the degree of
Master of Applied Science

Ottawa-Carleton Institute for Electrical and Computer Engineering
School of Electrical Engineering and Computer Science
University of Ottawa

IN LOVING MEMORY OF MY MOTHER AND FATHER
WHO
HAVE NEVER STOPPED ASKING ALLAH TO BLESS
ME
WHETHER
IN LIFE OR AFTER THEIR DEATH

ACKNOWLEDGMENTS

I would like to express my deep sense of gratitude to my supervisor Professor Trevor J. Hall for his valuable guidance and support throughout the development of this research. Words cannot express the value of his inspiring ideas, guidance and inexhaustible patience. I am gratefully indebted to him for generously providing all of the major elements needed to realize this achievement. Working with Professor Hall is indeed both a pleasure and an honor.

I am also grateful to my second advisor Dr. Sawsan A. Majid for her immeasurable contributions, suggestions, encouragement and support throughout the development of this research.

I also owe a debt of gratitude to the following colleagues: Tom Davies from Photon Design, Ramon Maldonado-Basilio from our Photonics Technology Laboratory, Imed Zine-El-Abidine from CMC Microsystems and Dr. Winnie Ye from Carleton University. They have generously contributed in providing feedback, support and encouragement during the course of achieving this study

To my fellow researchers, colleagues and professors Dr. Henry Schriemer, Dr. Karin Hinzer and Dr. Jianping Yao; to whom I had the pleasure of attending their courses specialized in photonics. Thank you to all of our administrative personnel for all of the facilities they provided to bring this work to reality.

I would also like to thank my family, my wife Nada Hammady, my sons Mohammed and Hussein, and our immediate family, especially my mom who died during the course of achieving this research, for their patience, encouragement, support, warm feelings and wishes that really helped me to accomplish this achievement.

Finally, I express my deepest and most sincere gratitude to Allah, the Most Gracious; the Most Merciful, and to the messenger of Allah Prophet Mohammed and the family of his house (Ahl al-Bayt); prayers and peace of Allah be upon them.

ABSTRACT

This thesis presents an introduction to the design and simulation of a novel class of integrated photonic phased array switch elements. The main objective is to use nano-electromechanical (NEMS) based phase shifters of cascaded under-etched slot nanowires that are compact in size and require a small amount of power to operate them. The structure of the switch elements is organized such that it brings the phase shifting elements to the exterior sides of the photonic circuits. The transition slot couplers, used to interconnect the phase shifters, are designed to enable biasing one of the silicon beams of each phase shifter from an electrode located at the side of the phase shifter. The other silicon beam of each phase shifter is biased through the rest of the silicon structure of the switch element, which is taken as a ground. Phased array switch elements ranging from 2×2 up to 8×8 multiple-inputs/multiple-outputs (MIMO) are conveniently designed within reasonable footprints native to the current fabrication technologies.

Chapter one presents the general layout of the various designs of the switch elements and demonstrates their novel features. This demonstration will show how waveguide disturbances in the interconnecting network from conventional switch elements can be avoided by adopting an innovative design. Some possible applications for the designed switch elements of different sizes and topologies are indicated throughout the chapter. Chapter two presents the design of the multimode interference (MMI) couplers used in the switch elements as splitters, combiners and waveguide crossovers. Simulation data and design methodologies for the multimode couplers of interest are detailed in this chapter. Chapter three presents the design and analysis of the NEMS-operated phase shifters. Both simulations and numerical analysis are utilized in the design of a 0º-180º capable NEMS-operated phase shifter. Additionally, the response of some of the designed photonic phased array switch elements is demonstrated in this chapter. An executive summary and conclusions sections are also included in the thesis.

CONTENTS

LIST OF FIGURES

CHAPTER 1 FIGURES

CHAPTER 2 FIGURES

CHAPTER 3 FIGURES

LIST OF ABBREVIATIONS

SOI	Silicon-on-Insulator
PIC	Photonic Integrated Circuit
IPPAS	Integrated Photonic Phased Array Switch
MMI	Multimode Interference
PTLab	Photonic Technology Laboratory
MZI	Mach-Zehnder Interferometer
NEMS	Nano-electromechanical Systems
WDM	Wavelength Division Multiplexing
FDM	Finite Difference Mode
3D	Three Dimensional
FV	Full Vectorial
MIMO	Multiple-Inputs Multiple-Outputs
I/O	Input/Output
EIM	Effective Index Method

LIST OF COLLIGATED PUBLICATIONS

Articles in Academic Journals:

[P1] **Ali A. Hussein**, Sawsan A. Majid and Trevor J. Hall, "Design of compact tunable wavelength division multiplexing photonic phased array switches using nano-electromechanical systems on a silicon-on-insulator integration platform," Optical and Quantum Electronics (OQE), submitted on September, 2013. (6 pages)

[P2] Saod A. Alseyab, **Ali A. Al-wasfi**, Abdulkareem S. Abdullah, "A Study of Steering Capability of a Microstrip Phased Array Using Inter-Injection Locked Oscillators," International Journal of Electronics, Vol. 75, No. 6, pp. 1221-1241, 1993. (21 pages)

Refereed Conference Proceedings:

[P3] **Ali A. Hussein**, Sawsan A. Majid and Trevor J. Hall, "Design of a Compact Tunable Wavelength Division Multiplexing Photonic Phased Array Switch Using Nano Electromechanical Systems on a Silicon-on-Insulator Integration Platform," NUSOD 2013 Conference (13th International Conference on Numerical Simulation of Optoelectronic Devices), University of British Columbia, Vancouver, Canada, August 19-22, 2013. (2 pages)

[P4] **Ali A. Hussein**, Sawsan A. Majid and Trevor J. Hall, "Design, Simulation and Fabrication of Nano-scale Silicon-on-Insulator (SOI) Integrated Photonic Phased Array Switch Elements (IPPAS) Utilizing Nano Electromechanical Systems (NEMS)," Proc. of SPIE, Vol. 8915, pp. 89150W-1 to 89150W-14, Photonics North Conference, Ottawa Convention Centre, Ottawa, Canada, June 3-5, 2013. (14 pages)

[P5] DeGui Sun, Imad Hasan, Sawsan Abdul-Majid, Rob Vandusen, Qi Zheng, **Ali Hussien**, Chunxia Wang, Zhongming Hu, T. Garry Tarr and Trevor J. Hall, "Performance Improvement to Silicon-on-Insulator Waveguide Directional-Coupler Based Devices," Proc. of SPIE, Vol. 7847, Optoelectronic Devices and Integration III, 78470F, November 17, 2010.

Presentations:

[P6] **Ali A. Hussein**, Sawsan A. Majid and Trevor J. Hall, "Design of a Compact 4×4 Photonic Phased Array Switch Using Nano Electromechanical Systems on a Silicon-on-Insulator Integration Platform," TEXPO 2013 Research Competition and Exhibition, Hilton Lac Leamy Hotel, Gatineau, Quebec, Canada, October 15-16, 2013.

[P7] **Ali A. Hussein**, Sawsan A. Majid and Trevor J. Hall, "Design of a Compact Micro-Size 2 × 2 SOI MMI Tapered Coupler," TEXPO 2011 Research Competition and Exhibition, Hilton Lac Leamy Hotel, Gatineau, Quebec, Canada, October 19-20, 2011.

EXECUTIVE SUMMARY

In this research, novel silicon-on-insulator (SOI) integrated photonic phased array switch (IPPAS) elements are proposed, designed and simulated. Fabrication of prototypes IPPAS designs, using the CMC Microsystem's NanoSOI nanomachining manufacturing process, is progressing. Prototype chips will be tested using the facilities in the Photonic Technology Laboratory (PTLab).

The IPPAS architecture may be considered as a generalization to N×N-ports of the traditional 2×2 Mach-Zehnder interferometer (MZI) switch element. The MZI traditionally has two photonic inputs and two photonic outputs. It comprises two 2×2 couplers that may be implemented as 2×2 MMI (multimode interference) couplers, one to act as a splitter (the input MMI coupler) and the other one to act as a combiner (the output MMI coupler). The two outputs of the splitter MMI coupler are connected to the two inputs of the combiner MMI coupler through electrically-controlled photonic phase shifters. The operation of these phase shifters is traditionally based on the thermo-optic effect, the carrier dispersion effect or the electro-optic effect. Each of these phase shifting techniques has its merits and demerits, but in general they all result in bulky elements placing a limit on the ambition to create complex photonic integrated circuits (PICs).

In general, an IPPAS consists of an input N×L MMI coupler, an output L×M MMI coupler, possibly a number of intermediate MMI couplers as needed and L interconnecting waveguide arms containing an electrically-controlled phase shifters. In this research, the phase shifters are implemented as nano electromechanical systems (NEMS) employing suspended slot waveguides with electrostatically controlled variable slot width. NEMS-operated phase shifters have a much smaller footprint compared to the orthodox thermo-optic or electro-optic phase shifting methods, and they do not require doping of the silicon saving both design area and manufacturing expense. The length of the NEMS-operated slot waveguide phase shift element designed in this work is 349 µm, whereas the length of an orthodox phase shift element in silicon length is in the millimeter range. The NEMS-operated phase shift elements offer a small capacitive load to the drive circuitry requiring little energy to operate. Innovative straight transition slot couplers, having a constant slot

width of 100 nm, are designed in this work to couple the NEMS-operated phase shifters to the interconnecting nanowire waveguides. The designed transition slot couplers are efficient; having optical mode coupling efficiency of around 97% based on simulation, and they provide the capability to bias the voltage-controlled phase shifter from one side resulting in compact size and neatness of the switch element. Additionally, all the MMI couplers of all sizes are designed such that the pitch size between the centers of their adjacent ports is the same (fixed to 2 µm). This permits the alignment of the phase shifter elements and their waveguide interconnections with the ports of the input/output (I/O) MMI couplers, which eliminates the need to use waveguide bends and the impairments of excess footprint, excess bend loss, and the relative phase error impairments they introduce. Phased array switch elements consisting of a NEMS-operated phase shift element array between compatibly dimensioned MMI couplers have not previously been described in the literature. In this work, they have been proposed and enable the construction of large-scale, ultra-compact size and ultra-small power consumption switch elements. IPPAS elements are a potentially suitable technology in a number of vital applications including signal routing, modulation, detection, signal processing and wavelength division multiplexing (WDM).

Integrated SOI-IPPAS circuits of different sizes including 2×2, 2×4, 4×4, 4×8 and 8×8 have been designed in full. Three core chapters are included in this thesis. Chapter (1) provides an introduction to IPPAS elements. Schematic diagrams for IPPAS elements ranging from 2×2 to 8×8 are outlined illustrating strategies to bring the active phase shift elements to either side of the circuit to facilitate electrical contacting. Typical design dimensions are indicated on these diagrams. Near vertical grating couplers are assumed in the presented schematic diagrams of the designed IPPAS elements to couple the light in and out of each switch element. However, edge coupled circuits have also been designed but not included in this particular chapter. Chapter (2) deals with the design and simulation of the MMI couplers used in IPPAS elements. A -3dB 2×2, crossover 2×2, -6dB 4×4, -3dB 4×4 and -9dB 8×8 couplers are designed to typical performance parameters. MMI couplers rely on producing self-images at the output ports. Both minimum excess losses and minimum imbalances are desired. The MMI couplers are optimized for a minimum cost that combines and can trade-off excess loss and imbalance. Chapter (3) presents the design and simulation of the NEMS-operated cascaded slot waveguide phase shifters. The transmission-phase response of some of the designed IPPAS elements to some defined phase synthesis modes applied to the NEMS-operated phase shifters is also included in this chapter. Testing strategies, results of laboratory verification, targeted applications of the IPPAS fabrics and prototyping of some design variations is underway.

The tool used to verify the design of the IPPAS components is FIMMPROP from the Photon Design suite of simulation tools. The simulations made use of the complex finite difference mode (FDM) three-dimensional (3D) full vectorial (FV) eigenmode solvers of FIMMPROP. Accurate simulation data is obtained using these solvers. A combination of custom numerical analysis code and simulation tools has been used to design the NEMS slot-waveguide phase shift elements. The scattering parameters of the different fabric components obtained from simulation are used to predict the transmission-phase response of the studied IPPAS elements. Testing plans have been established and the proposed methods are being verified. The testing is mainly targeting estimating losses and imbalances, verifying the phase differences achieved by the NEMS phase shift elements and qualifying the output states of the circuits. Testing strategies based on both the interferometry inherent in the structure and methods based on spectral interferograms produced by the intentional introduction of path imbalance are being investigated.

CHAPTER 1

INTRODUCTION TO PHOTONIC PHASED ARRAY SWITCHES

1.1 Abstract

This chapter introduces the concept of the photonic phased array switch elements. The chapter starts with an overview of the IPPAS elements addressing the components used in building this type of PICs and indicating their novel features. The principle of operation of the NEMS-operated phase shifter of cascaded under-etched slot waveguides is indicated revealing its advantage compared to other alternate phase shifting methods. An explanation of the SOI integration platform utilized in building the IPPAS testing structures is briefly included. Then, the schematic diagrams of the designed IPPAS elements of different sizes ranging from 2×2 to 8×8 are presented with detailed dimensions indicated on them. The IPPAS elements presented in this chapter assume broadband responses where the waveguide paths of the network interconnecting the splitter/combiner MMI couplers have all the same length for any particular IPPAS element. In consequence, no waveguide bends are needed in the network part between the splitter/combiner MMI couplers. Some possible applications of the IPPAS elements are associated in this chapter.

1.2 Overview of Photonic Phased Array Switches

Photonic phased array switch elements integrated on silicon on insulator material platform (SOI-IPPAS) are versatile photonic integrated circuits (PICs) with a multiple-input multiple-output (MIMO) structure that create amplitude-phase relations between their ports parameterized by the phase shifts induced by external voltage applied to a phase shift element array. IPPAS may be considered to be a generalization of the traditional MZI modulator. The traditional MZI modulator has two photonic inputs and two photonic outputs with a structure consisting of two 2×2 couplers interconnected by a dual phase modulator. IPPAS elements in contrast employ a N×L multimode interference (MMI) coupler at the input and a L×M MMI coupler at the output interconnected with an array of L phase shift elements. Usually N = L = M but this is not a necessary condition and there are advantages to structures with L > M.

Thermo-optic, carrier dispersion effect or electro-optic effects have been deployed to implement the phase shifting elements in traditional MZI modulators described in the literature. The thermo-optic phase shifting effect is effective but slow and dissipates a large amount of electrical power. The carrier dispersion effect is fast but is weak and introduces excess losses. The electro-optic effect is fast but weak and only available in certain material platforms. The focus of this work is on silicon which possesses no linear electro-optic effect. These traditional phase shifting elements have large foot prints (~mm^2) consuming an excessive proportion of the available chip area. They usually require electrical contacts (electrodes) on both sides of each phase shifter forcing the placement of the phase shifters in a photonic phased array away from each other, usually in one column, such that waveguide bends have to be used to accommodate the resulted structure enticing additional loss, exacerbating the chip area consumed and entailing greater difficulty controlling the path lengths of the interconnections between the input/output (I/O) MMI couplers. Waveguide crossovers might also be needed to realign the electrodes on the sides of the fabric at the expense of increased insertion loss and cross-talk. This in consequence puts a cap on the objective of constructing large photonic phased array switch fabrics that can be implemented using existing fabrication technologies such as the silicon photonics processes.

In this research, the phase-shift elements are implemented as nano electromechanical systems as an alternative to the traditional approaches. The NEMS phase shift elements use suspended slotted photonic waveguides with an electrostatically controlled variable slot width. The slotted photonic wire in essence consists of two nanoscale silicon beams with sub-micron separation (100 nm) that are rendered free to move laterally relative to each other by using an under-etch step in the fabrication process to remove the oxide layer underneath the silicon beams. Applying a voltage to the freestanding beams changes the slot width between the silicon beams which in its turn results in a strong variation of the effective index of the slot waveguide. By utilizing a sufficient number of NEMS-operated slot waveguide sections in cascade, a micro-size phase shift element with 15 cascaded slot waveguide sections has been designed in this work that is capable of 0º-to-180º at about 0-to-15 V of applied voltage; a fundamental resonant frequency of the nano-mechanical structure of about 50 MHz; and a pull-in voltage of about 17.7 V. The NEMS-operated phase shift element requires significantly less chip area, only 349 µm in length, and uses much less power, in the micro Watt range, compared to other phase shifting approaches. The only current needed to modulate the gap width between the freestanding silicon beams is due to the charging of the capacitance effect between them, which is estimated in the femto Farad range. The design of the NEMS-operated slot waveguide phase shifter is based on the numerical approach presented by Acoleyen et al. [1] and the simulation of the effective index of the slot wire using FIMMPROP. Acoleyen designed, fabricated and tested a NEMS-operated phase shifting line of three cascade slot waveguides. Acoleyen's phase shifting line achieved up to about 40º. Acoleyen's experimental measurements showed that the electromechanical behavior of the NEMS-operated slot nanowire is located (about midway) between fixed and hinged boundary conditions of the freestanding silicon beams.

One novel aspect of this research is the incorporation of the NEMS-operated phase shift element into practical phased-array switch PICs. A second novel aspect is a highly efficient straight transition slot nanowire coupler that has not been previously described in the literature that has been designed to couple the I/O single mode nano waveguides to the NEMS-operated phase shifter of cascaded slot waveguides. The distinguishing feature of this transition slot nano waveguide coupler is that it enables direct electrical connection to one of the silicon beams of the NEMS-operated phase shifter through the rest of the silicon system components to the common ground electrode, whereas the other silicon beam of the slotted wire phase shift element is excited through a separate electrode. Therefore, one separate electrode is needed per NEMS-operated phase shifter used in IPPAS fabrics compared to two using other approaches. Simulation using FIMMPROP showed that the designed transition slot coupler has optical mode coupling efficiency of about 97%. In addition, all the MMI couplers used in the proposed photonic phased array switches are designed so that the centers of their I/O access ports have the same pitch. This eliminates the need to use waveguide bends between the I/O MMI couplers, eliminating a source of excess footprint and relative path-length imbalance. Finally, a special arrangements, proposed for the first time, brings the internal waveguides interconnecting the I/O MMI couplers to the exterior to connect to their phase shift element and enables all the NEMS-operated phase shifter elements to be placed only at the exterior sides of the structures which facilitates electrical contacting. These novel arrangements help to reduce the total loss of the system, better organize the components within the circuit, and facilitates the design and fabrication of larger scale systems.

IPPAS fabrics are candidate solutions for many applications including: direct routing of photonic signals; photonic modulators and detectors; processing of photonic signals; RoF (radio-over-fiber) applications; filtering of photonic signals and processing of electronic signals using PICs. IPPAS elements can provide both amplitude and phase modulation to the input photonic signals. The versatility of the I/O amplitude-phase relations depends on the complexity of the photonic switch element. In this work 2×2 (the basic MZI configuration), 2×4, 4×4, 4×8 and 8×8 switch elements have been designed. The photonic switch element consists of MMI couplers (usually an input and output MMI couplers and possible intermediate MMI couplers); a number of NEMS-operated phase shifters of cascaded slot waveguides depending on the number of interconnecting waveguide branches between the I/O MMI couplers; interconnecting single mode nano waveguides and tapers to adapt the width of the single mode waveguides to the width of the access ports of the MMI couplers. Additionally, near vertical coupling grating couplers or edge couplers are usually incorporated in the technology to enable input and output of the light. All system components including the MMI couplers, the NEMS-operated phase shifters, the single mode nano waveguides and the tapers have been designed to typical specifications.

The complex FDM-3D-FV solver of the FIMMPROP software is used in simulation which means high accuracy in achieving design parameters. Accurate procedures have been utilized in design details. Taking an example, the -6dB 4×4 MMI coupler designed in this work is smaller than that designed by Voigt [2] in a recent research for comparable excess loss and imbalance. The -3dB 2×2 MMI coupler designed in this work exhibit small excess loss of 0.11 dB and minimal imbalance of 0.053 dB. A variety MMI couplers are designed to typical performance parameters and utilized in the IPPAS fabrics including a -3dB 2×2, -6dB 4×4, -9dB 8×8, crossover 2×2 and -3dB 4×4. Up to the author’s knowledge, 8×8 MMI couplers are rarely deployed in practical photonic systems. All parameters including imbalance, excess loss, scattering parameters and optical power distribution have been simulated for the different designed components. Simulations of the NEMS-operated phase shift element consisting of 15 cascaded slot waveguides together with the transition slot waveguide couplers show a typical total excess loss of about 1.1 dB. Each additional cascade slot waveguide is estimated to cost about 0.055 dB of excess loss based on simulation results. The simulated scattering parameters of the designed components are used to predict the I/O amplitude-phase relations of the different IPPAS circuits and to trial different applications.

The proposed IPPAS elements presented here have been designed to the smallest details. CMC Microsystems have granted us access to their NanoSOI nanomachining fabrication process to prototype some IPPAS elements design variants on a SOI wafer with a silicon thickness of 300 nm and minimum feature size of 100 nm. Testing of the designed IPPAS chips is planned to be conducted in our PTLab. The designs may be adapted as needed in future, simply and in a reasonably short time, to other fabrication processes such as the IMEC process , which uses a 220 nm of silicon thickness, or even the 145 nm of silicon thickness option a of the NanoSOI nanomachining manufacturing process of CMC Microsystems. The MZI inherent in the designed structures enables the evaluation of the phase shift difference achieved by the NEMS-operated phase shifter of cascaded slot waveguides and the study of the transmission characteristic of the IPPAS circuits. Development of the test plan based on both the MZI interferometry and spectral interferometry is being investigated. Testing of the designed nanophotonic components and systems is of great importance to evaluate their performance and to close the gap of uncertainty due to the approximations involved in numerical procedures and manufacturing tolerances of nanostructures and it is vital to design prototypes to facilitate the test procedures (i.e. design-for-test).

1.3 Nanophotonic Silicon-on-Insulator Platforms

The SOI photonic integration platform offers very tight light confinement due to the high contrast between the refractive index of the silicon core layer and the refractive index of the surrounding cladding. The SOI platform has therefore become the first choice for designers seeking passive components and circuits with small footprints. The possibility of etching the buried oxide layer under the silicon nanowires provides an opportunity to extend the applications of SOI platforms to include active devices based on the NEMS-operated slotted waveguides. Active SOI platforms are promising in many applications including switching, modulation, detection and photonic signal processing. Additionally, active SOI platforms can result in compact ultra-low power consumption PICs manufactured in low price technology.

Figure 1.1 illustrates the layers of an SOI platform. The light is confined in the silicon core layer which typically has a refractive index of about 3.45. The silicon core layer is sandwiched between the oxide layer underneath it and usually air on top of it. The oxide layer has a typical refractive index of about 1.44 and the air layer has a refractive index of 1. The thickness of the oxide layer is usually in the range of 1 μm to 2 μm. The thickness of the silicon core layer, on the other hand, has been standardized to a small number of fixed values suited to the fabrication technology. The Inter-university Micro-Electronics Centre (IMEC) SOI nanophotonic platform conveniently uses a typical silicon layer thickness of 220 nm. The CMC Microsystems NanoSOI nanomachining manufacturing process has two convenient SOI platforms with two different silicon core thicknesses of 145 nm and 300 nm. Changing the thickness of the silicon core implies different dimensions for overall structure of components and requires redesigning and the running of new simulations.

In this research, the silicon base layer thickness of 300 nm of the CMC Microsystems Soitech platform is adopted for the designs. Checking of the performance changes based on the other aforementioned available platforms is left for future work. The silicon core layer is supposed to be fully etched to form the boundaries of the designed photonic structures. Shallow etching (e.g. about 70 nm deep for IMEC) can also be employed to construct the near vertical grating couplers used to externally access the on-chip fabrics. Another important parameter in designing SOI structures is the minimum feature size, which refers to the smallest design detail that can be manufactured. The minimum feature size for the aforementioned manufacturing technologies is typically 100 nm or less. The slot width of the NEMS-operated slot nanowires is 100 nm matching this limitation.

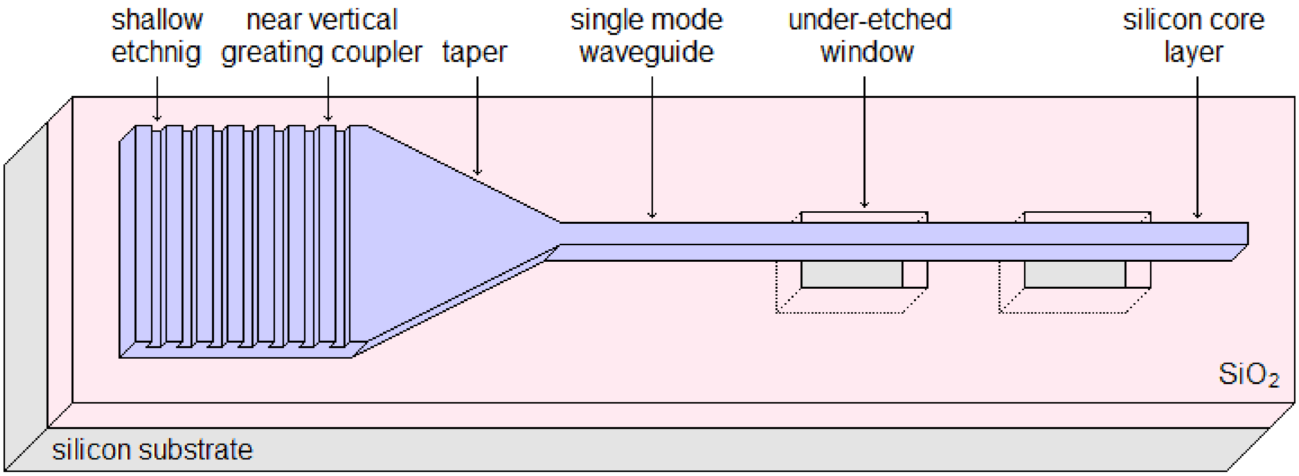

Figure 1.1 Silicon-on-insulator technology.

1.4 Layout of Ordinary Photonic Phased Array Switches

Figure 1.2 shows a schematic diagram for an ordinary layout of a 4×4 IPPAS switch element. Two 4×4 MMI couplers are used in this switch element. Each branch connecting one of the outputs of the MMI coupler splitter to one of the inputs of the MMI coupler combiner has a traditional electro-optic or thermo-optic phase shift element in its path. The single mode waveguide paths interconnecting the I/O MMI couplers and the phase shifters are routed so that the lengths of the four different paths between the I/O MMI couplers are all the same. This ensures each path provides the same phase shift when the phase shifters are biased at zero.

Each traditional phase shift element is bulky. The electrodes required on either side of the device for bias present particular layout difficulties. Waveguide crossovers in a multistage circuit might be used to bring interior electrodes to the exterior of the circuit but at the cost of increased layout complexity. The electrodes are required to be spaced well away from each other to physically facilitate accessing them and also to control the gradient in the electric field potential developed between the electrodes at micrometer range distances.

Waveguide bends are needed to accommodate the disparity in footprint between the MMI couplers and the phase shift elements. These introduce additional losses; consume footprint and are a potential source of path length imbalance resulting in more difficulties to implement large dimension switches. The location of the electrodes create difficulties for test procedures as they are located in the midst of the structure between the input and output coupling ports and require more difficult multilayer wiring arrangements (not a plane single layer layout). The near vertical grating couplers are needed to couple the light between the probing fibers and the IPPAS switch. Tapers are used to adapt the width of the interconnecting single mode waveguides to the width of the MMI coupler ports.

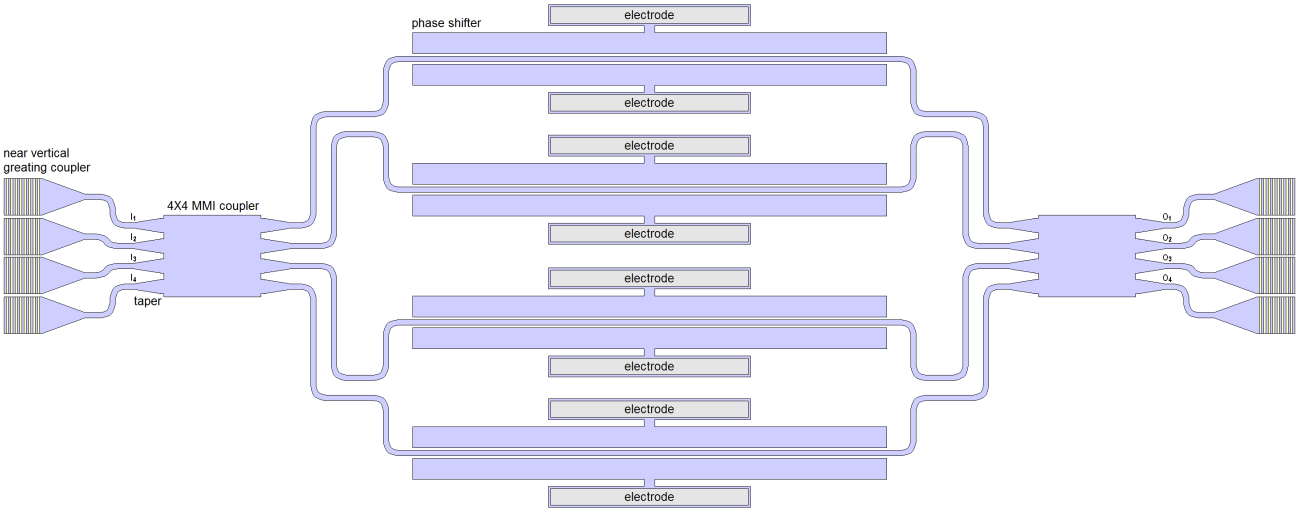

Figure 1.2 Layout of an ordinary 4×4 IPPAS element.

1.5 Outline of a 2×2 Photonic Phased Array Switch Element

Although, a 2×2 IPPAS element shares the characteristic of a traditional MZI modulator, it inherits the distinct novel features of the IPPAS class of switch elements. Figure 1.3 shows the schematic diagram of the 2×2 IPPAS element introduced in this work. The switch element consists of two -3dB 2×2 MMI couplers with two NEMS-operated phase shifters interconnecting them. A -3dB 2×2 MMI coupler splits the optical power at an entrance port equally into the two arms. The optical beams in the two arms of phase shift elements recombine at the exit -3dB 2×2 MMI coupler arms. The phase shift elements in the two arms adjust the interference of the two beams on recombination such that light may be switched between either one of the two output ports of the switch element. This basic switch element is also characterized by the capability to change the phase modulation due to voltage applied at the electrodes of the fabric into both amplitude and phase modulation of the light transferred through the silicon fabric.

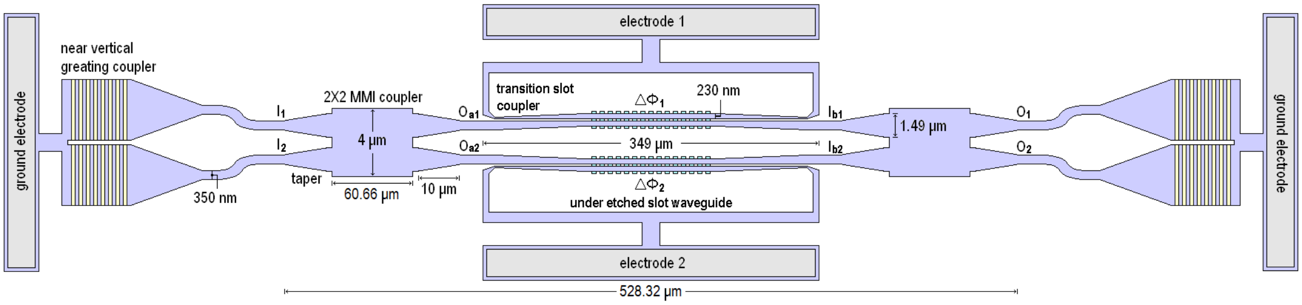

Figure 1.3 Schematic diagram of a 2×2 IPPAS element.

The NEMS-operated phase shifter used in the switch element is composed of 15 cascaded slot waveguides estimated to provide a phase shift of more than 180° at an applied voltage of about 15 V. The switch element uses no waveguide bends in the interconnecting branches between the ports of the MMI couplers. Near vertical grating couplers or edge couplers can be used to couple the light in and out the switch fabric. One of the silicon beams of each NEMS-operated phase shifter is connected to the common ground electrode through the rest of the silicon waveguide circuitry as outlined in the figure. The other silicon beam is connected to an isolated electrode located on one side of the phase shift element. This switch element is compact in size, has a simple layout and it may provide an ideal system to measure the phase difference introduced by the NEMS-operated phase shifters using the MZI-like behavior.

In Figure 1.3, $\Delta\phi_1$ and $\Delta\phi_2$ are the phase shift differences introduced by the two NEMS-operated phase shifters due to the external voltage applied to electrodes 1 and 2, respectively. The length of the NEMS-operated phase shifter with the I/O straight transition slot waveguide couplers is 349 µm. The entire length of the core of the switch element of this figure excluding the I/O coupling arrangements to the optical fibers of near vertical grating couplers, tapers and adjusting waveguide bents is 528.32 µm. This length is much smaller than that of a traditional MZI modulator; the length of a traditional phase shift element alone is in the millimeter range.

1.6 Outline of a 2×4 Photonic Phased Array Switch Element

Replacing the 2×2 MMI combiner in Figure 1.3 with a 4×4 MMI coupler, a 2×4 switch element with the topology depicted in Figure 1.4 is obtained. This switch fabric is composed of a -3dB 2×2 MMI coupler, a -6dB 4×4 MMI coupler, two NEMS-operated slot waveguide phase shifters and the interconnecting structure of single mode nanowires and tapers. An input applied to the -6dB 4×4 MMI coupler produces all four equal power outputs. This particular fabric can operate as a two-way switch, where either one of the two inputs might be switched to either one of two different outputs simultaneously.

The core length of this IPPAS element is 589.86 µm as indicated in Figure 1.3. It also represents one of the simple circuits suited to the measurement of the phase shift characteristic of the NEMS-operated phase shift elements. Replacing the combiner -6dB 4×4 MMI coupler with a -3dB 4×4 MMI coupler yields a switch element with different response. A -3dB 4×4 MMI coupler produces two equal power outputs due to one of its inputs and will be explained in detail in Chapter (2). It is also possible to replace the splitter -3dB 2×2 MMI coupler with a crossover 2×2 MMI coupler and redirect the respective outputs of the NEMS-operated phase shifters to inputs I_{b1} and I_{b3} of the combiner -6dB 4×4 MMI to manipulate a coherent 90º optical hybrid with active phase shift modulation capability. The operation modes corresponding to redirecting the outputs of the NEMS-operated phase shifters to different combinations of the combiner 4×4 MMI coupler inputs (i.e. I_{b1} through I_{b4}) are different. However, choosing two adjacent inputs of the combiner 4×4 MMI coupler eliminates the need to use waveguide bends in the core of the circuit. Investigating the response of these architectural design variations is targeted.

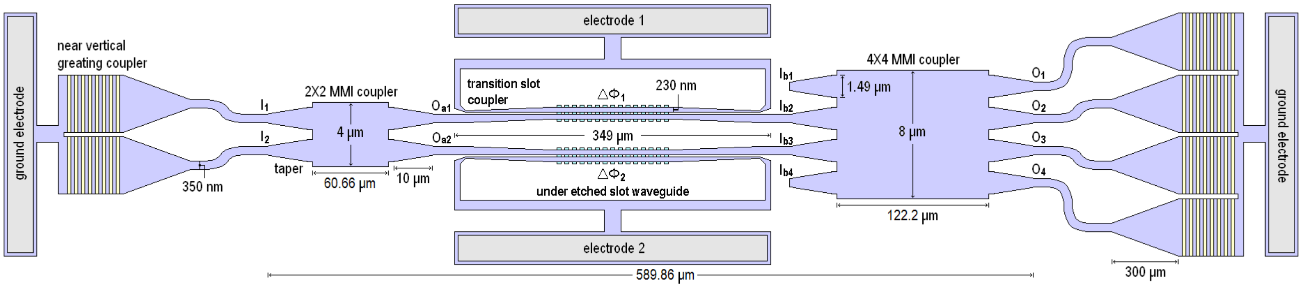

Figure 1.4 Schematic diagram of a 2×4 IPPAS element.

1.7 Outline of a 4×4 Photonic Phased Array Switch Element with Two Phase Shifters

A 4×4 IPPAS element implemented using two 4×4 MMI couplers with four branches interconnecting them but with using only two NEMS-operated phase shifters located on the sides of the structure is shown in Figure 1.5. The active NEMS-operated phase shifters contribute to phase differences only to the outer interconnecting branches running between the MMI couplers. As shown in the figure, the two inner interconnecting braches between the MMI couplers have passive non-activated NEMS-operated phase shift structures identical to the active ones. The reason for adding these passive phase shifters is to ensure all of the four branches interconnecting the MMI couplers are matched.

Due to the fact that only two active phase shifters are used in this 4×4 fabric, using -6dB 4×4 MMI splitter and combiner couplers might not enable this fabric to fully switch the inputs to isolated outputs. However, modulation/demodulation applications are still possible. Alternatively, replacing the input splitter with a -3dB 4×4 MMI coupler and keeping the -6dB 4×4 MMI combiner can roll-back this circuit to a 2×4 switch element type utilizing only the outer inputs (I_1 and I_4). A two-way switch fabric is expected in this case with the possibility of a coherent detection capability.

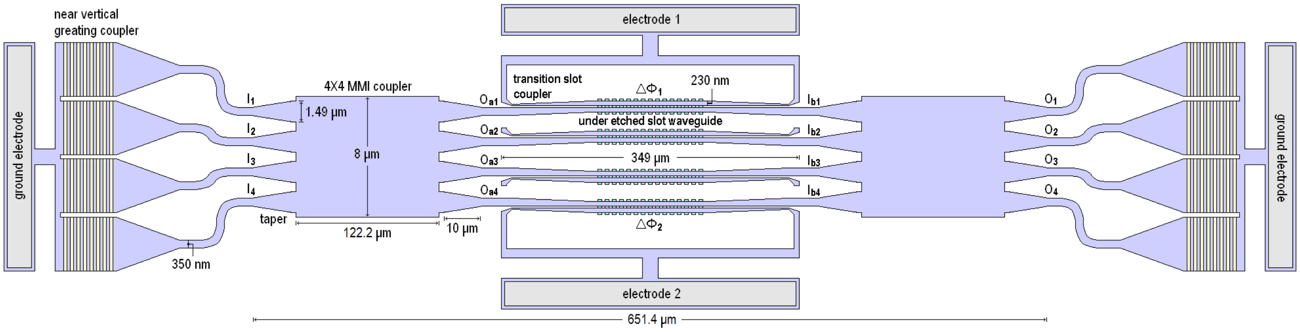

Figure 1.5 Schematic diagram of a 4×4 IPPAS element with two phase shifters.

1.8 Outline of a Full 4×4 Photonic Phased Array Switch Element

A full size 4×4 IPPAS switch element is shown in Figure 1.6. This switch element has four NEMS-operated phase shifters. Each phase shifter is attached to one of the four branches interconnecting the I/O MMI couplers. Two intermediate crossover 2×2 MMI couplers are used to toggle the interconnecting paths such that all of the four phase shifters are located on the sides of the fabric as seen in the figure. The interconnecting paths are interlaced with each other as they are connected to the combiner MMI coupler. That is O_{a1}, O_{a2}, O_{a3} and O_{a4} are connected to I_{c2}, I_{c1}, I_{c4} and I_{c3} through $\Delta\phi_1$, $\Delta\phi_2$, $\Delta\phi_3$ and $\Delta\phi_4$, respectively. This switch element provides full switching capability with the use of -6dB 4×4 splitter and combiner MMI couplers. It is also possible to replace either one or both of the I/O MMI couplers with -3dB MMI couplers resulting in different response IPPAS elements.

As indicated in Figure 1.6, the length of the core of this switch element with the -6dB MMI couplers is 1128.95 µm, which is possibly still shorter than just the length of a traditional electro-optic or thermo-optic phase shift element. It should be mentioned here that the inner edges of the crossover 2×2 MMI couplers are separated from each other by a distance of 0.51 µm; quite enough to avoid direct coupling of their internal fields. The pitch size between the centers of the adjacent I/O ports of the intermediate crossover 2×2 MMI couplers is the same as those for the I/O MMI splitter and combiner. Thanks to this novel feature in the design, the need to use any waveguide bends to interconnect the I/O MMI couplers is eliminated. The electrodes are spaced from each other sufficiently that the electric field intensities developed between them when applying external voltages remain within safe limits. This 4×4 switch design inherits the MZI-type behavior but exceeds it in switching and modulation capabilities. Its compact footprint, good organization, IC like terminals, mask design simplicity, ultra-low power consumption and low excess loss can make it a preferred choice in contemporary photonic systems.

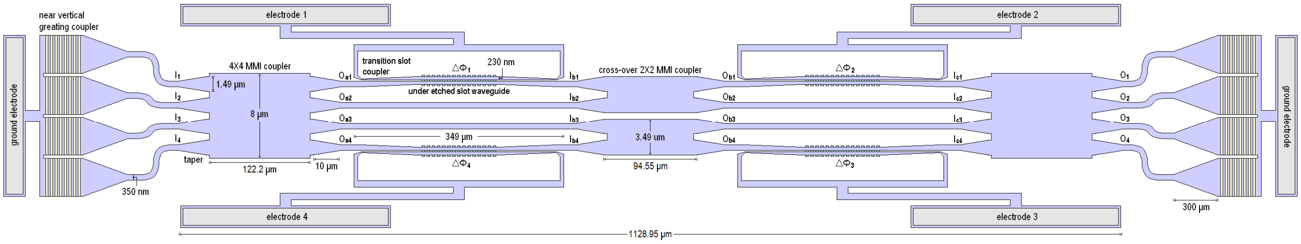

Figure 1.6 Schematic diagram of a 4×4 IPPAS element with all paths phase shifters.

1.9 Outline of a 4×8 Photonic Phased Array Switch Element

A 4×8 phased array switch element with each interconnecting path equipped with a separate NEMS-operated phase shifter is depicted in Figure 1.7. The interconnecting paths can be aligned to different combinations of the combiner 8×8 MMI coupler. However, using a sequential four inputs of the 8×8 MMI coupler avoids the need for waveguide bends between the MMI couplers. Multi-way switching capability is expected using this switch fabric. The figure shows the interconnecting paths adjusted exactly to the mid inputs of the 8×8 MMI coupler. The dimensions of a splitter -6dB 4×4 MMI coupler and a combiner -9dB 8×8 MMI coupler are indicated on the figure. With this choice, the core length of the 4×8 IPPAS fabric is 1252.5 μm as indicated in Figure 1.7. This length is still reasonable to manufacture with the currently available technologies. It is also possible to replace the -6dB 4×4 MMI coupler with the -3dB 4×4 coupler version to create a fabric with different function.

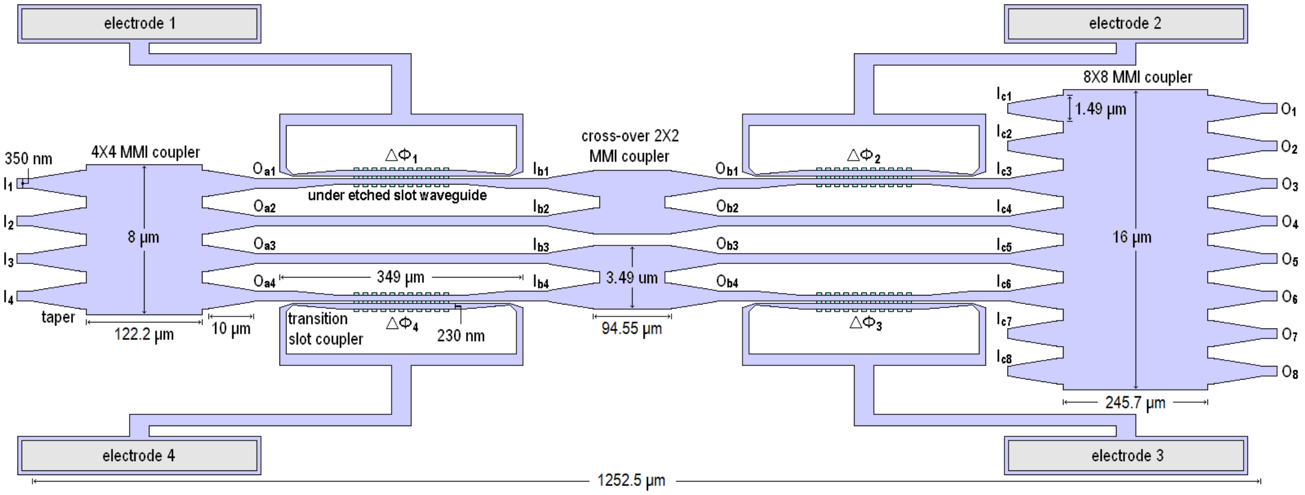

Figure 1.7 Schematic diagram of a 4×8 IPPAS element.

1.10 Outline of an 8×8 Photonic Phased Array Switch Element

An 8×8 IPPAS element equipped with eight separate phase shifters is depicted in Figure 1.8. This fabric provides full switching capability and versatile amplitude-phase relationships between its eight inputs and eight outputs. Twelve crossover 2×2 MMI couplers are used to arrange the eight separated NEMS-operated phase shifters on the sides of the circuit, one to each branch interconnecting one of the splitter 8×8 MMI coupler to one of the combiner 8×8 MMI coupler. The interconnecting branches are interlaced such that the outputs of the splitter 8×8 MMI coupler numbered from 1 to 8 are connected to inputs 4, 3, 2, 1, 8, 7, 6, and 5, respectively, of the combiner 8×8 MMI coupler.

The length of the fabric core with the I/O -9dB 8×8 MMI couplers shown in the figure is 2331 µm. This length, indeed, is currently challenging to manufacture. Therefore, this architecture will be mostly considered for theoretical study only and it could be targeted as a possible future milestone.

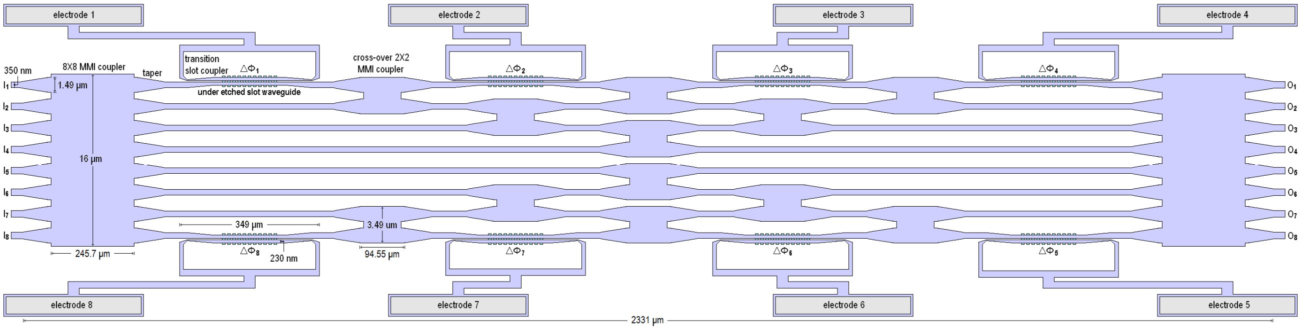

Figure 1.8 Schematic diagram of an 8×8 IPPAS element.

CHAPTER 2

ANALYSIS, DESIGN AND SIMULATION OF MICROSIZE SOI MULTIMODE INTERFERENCE COUPLERS

2.1 Introduction to SOI Multimode Interference Couplers

The excellent properties of SOI-MMI couplers, including compact size, low loss, low reflection, low crosstalk and wide bandwidth response, have encouraged the use of SOI-MMI couplers in a number of PICs. A Glance at the literature provides examples of application utilizing SOI-MMI couplers that include electro-optic switches [3,4], MZI-based switches [5,6], passive MZI polarization splitters and convertors [7], microring resonators [8], optical 90° hybrids [9-12] and phased array wavelength division multiplexers (WDMs) [13].

Tapers are usually used to adapt the width of the interconnecting single mode waveguides to the wider width of the I/O access ports of the MMI coupler. Controlling the width of the access ports to an MMI coupler is of great importance to optimize imbalances in the split ratios and excess losses for the different inputs to the MMI coupler [16]. The criteria of uniform split ratios and minimal excess loss has been faithfully satisfied in this work.

In this research, MMI couplers are used basically as splitters and combiners in IPPAS elements. Crossover MMI couplers are used also to interlace adjacent optical paths with each other as explained in Chapter (1) of the thesis. The design of a variety of MMI couplers of different types and different port dimension sizes is discussed in this chapter of the thesis including -3dB 2×2, crossover 2×2, -6dB 4×4, -3dB 4×4 and -9dB 8×8. All the MMI couplers presented in this chapter are simulated and designed at an operating optical center wavelength of $\lambda = 1550$ nm.

The design of MMI couplers rests on ensuring the production of self-images of the input access port field profiles at the output access ports. Optimum self-images result at minimum excess loss points.

The set of parameters that result in minimum imbalances and minimum excess losses for the different inputs of 4×4 and 8×8 MMI couplers do not exactly match each other. Optimization functions for the minimization of the non-uniformity in the output powers and the minimization of power losses for the different inputs of the MMI couplers of sizes 4×4 and 8×8 are formulated and used in design in this work.

The simplified theory of MMI couplers based on the effective index method (EIM) is presented in the next section. Although approximate, it provides the greatest insight into the physics of MMI couplers. The complex FDM-3D-FV solver of FIMMPROP is used in simulations to design the different MMI couplers used in this work. This work is based on high accuracy simulations and follows credible procedures to produce MMI couplers exceeding previously reported standards.

2.2 Analysis of SOI Multimode Interference Couplers

In this section we illustrate the analysis in terms of the 2×2 MMI coupler shown in Figure 2.1. The MMI coupler is rectangular with width W_c and length L_c. The entrance face of the MMI coupler is divided into two access sections each of width W_{am} corresponding to the absolute maximum possible access port width. Each I/O access port has width W_a and it is centered exactly at the midpoint of the access section. Linear tapers, each of length L_t, are used to adapt the width W_g of the access single mode access waveguides to the width of the access ports of the MMI coupler, W_a. The two inputs applied to the MMI coupler ports are respectively designated as I_1 and I_2. Similarly, the two outputs extracted from the MMI coupler ports are respectively designated as O_1 and O_2. A reversible design is assumed. The silicon core layer thickness is taken as 300 nm for simulation purposes as indicated in Chapter (1). Full etching of the silicon layer to the silicon dioxide layer is also assumed in this work.

Practically, the maximum width of the access port can be such that $W_a \leq W_{am}-2W_f$, where W_f is the minimum feature size that can be manufactured. In this work we seek the value of W_a within the range from W_g to $W_{am}-2W_f$ such that the imbalance in the split ratios is minimal.

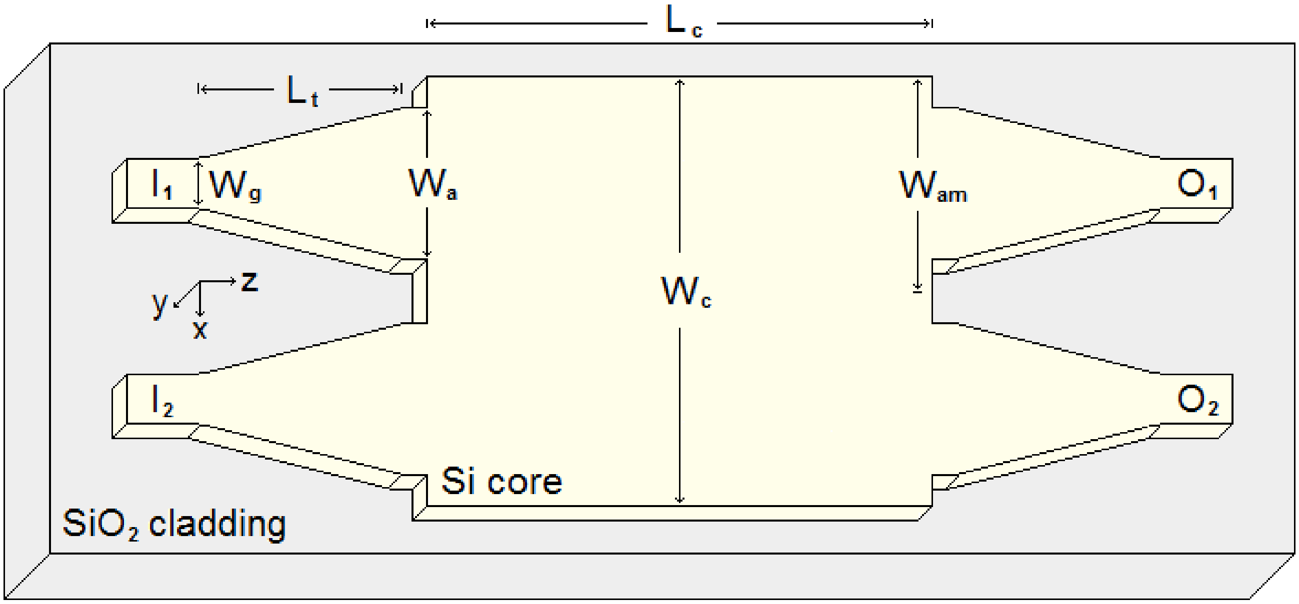

Figure 2.1 Geometry of a -3dB 2×2 MMI coupler.

The used separation between the adjacent waveguides and the relative dimensions of the adjacent tapers are confirmed through simulation not to cause any effective direct coupling between them. The length and width of the rectangular MMI coupler as well as the width of the access ports and their relative locations, indeed, determine the transmission coupling characteristic. An MMI coupler is designed such that the field profile of the input ports are reproduced at the desired output ports. The reproduced field profiles at the output ports are referred to as Talbot or self-images of the input field profiles [17,18]. Manufacturing tolerances and discrepancies from the assumptions of simulation cause deviations from reproducing perfect self-images at the output ports yielding non-zero imbalance and excess loss in actual MMI couplers.

Deep etching of the silicon structure maximizes the contrast in the refractive index profile between the core and the surrounding cladding. As a result, the penetration of the fields in the cladding is negligible. This in turn avoids uncertainty about the effective widths and equates them to the physical widths used in this analysis. The use of the EIM can reduce the analysis of the three-dimensional MMI coupler structure into a two-dimensional problem [17]. The normalized field profile at an input access port is assumed to correspond to the fundamental mode:

$$\psi_{in}(x) = \sin(\frac{\pi}{W_a} x) \tag{2.1}$$

The multimode section of the MMI coupler is assumed to support M eigen-modes. These modes are numbered with index $m = 0,1,\ldots,M-1$. The TE_m field profile of mode m can be described by [19,20]:

$$\psi_m(x,z) = C_m \sin(\kappa_m x) \exp(-j\beta_m z) \tag{2.2}$$

The time dependency, $exp(j\omega t)$, in Eq. (2) is implicit. κ_m and β_m are the transverse and longitudinal components of the propagation constant of the pair of plane waves that constitute the mode (i.e. the transverse and longitudinal spatial angular frequencies of the modal field) of mode m. Mathematically, the field distribution of each mode m is extended over the width $2W_c$ such that it is an odd function of the lateral x-direction in respect of the sidewalls. Each mode m has $m+1$ number of periods within the spatial interval $-W_c < x < W_c$. κ_m and β_m are given by:

$$\kappa_m = (m+1)\kappa, \quad \kappa = \frac{\pi}{W_c} \tag{2.3}$$

and in the paraxial approximation:

$$\beta_m = kn_e - \frac{\pi(m+1)^2 \lambda}{4n_e W_c^2} \tag{2.4}$$

$k = 2\pi/\lambda$ is the propagation constant in free space. λ is the free space wavelength. n_e is the effective index in the multimode region. At a distance z from the input access port, the phase difference ϕ_m between the mode m and the mode 0 is given by:

$$\phi_m(z) = -(\beta_m - \beta_0)z = \frac{\pi m(m+2)\lambda}{4n_e W_c^2} z \tag{2.5}$$

where Eq. (2.4) has been used. The beat length of the MMI section L_π is defined such that the phase shift between the two lowest order modes is π:

$$L_\pi = \frac{-\pi}{\beta_1 - \beta_0} = \frac{4 n_e W_c^2}{3\lambda} \tag{2.6}$$

where Eq. (2.4) has been substituted. Hence, ϕ_m of Eq. (2.5) can be expressed in terms of L_π as:

$$\phi_m(z) = \frac{\pi m(m+2)}{3L_\pi} z \tag{2.7}$$

The field profile in the MMI coupler, neglecting the progressive phase shift $exp(-j\beta_0 z)$, can be expressed as the Fourier series:

$$\psi(x,z) = \sum_{m=0}^{M-1} c_m \sin\left((m+1)\kappa x\right) \exp\left(j\phi_m(z)\right) \tag{2.8}$$

Eq. (2.8) shows that the field at any point inside the MMI coupler is the superposition of $2M$ interfering plane waves. The weight c_m, of the mode m, is the Fourier series coefficient due to the periodic odd field profile at the input access port (evaluated at $z = 0$):

$$c_m = \frac{2}{W_c} \int_{\frac{W_c}{4} - \frac{W_a}{2}}^{\frac{W_c}{4} + \frac{W_a}{2}} \psi(x,0) \sin\left((m+1)\kappa x\right) dx \tag{2.9}$$

Eq. (2.9) is written for input I_1. An analytical solution for the c_m weights can be derived from Eqs. (2.1) and (2.9) when needed. The inspection of Eq. (2.8) shows that single and multiple self-images of the input optical field are formed at the MMI coupler lengths, $L_c = 3L_\pi(p/q)$, where $p \geq 0$ and $q \geq 1$ are integers with no common divisor [20]. The integer q represents the number of images formed in the extended field. For a -3dB 2×2 MMI coupler, two self-images are formed at the shortest coupler length of value: $L_c = 3L_\pi/2$ (i.e. $p = 1$ and $q = 2$). For a crossover 2×2 MMI coupler, a mirrored single image is formed at the coupler length of value: $L_c = 3L_\pi$ (i.e. $p = 1$ and $q = 1$). For a -9 dB 4×4 MMI coupler, four self-images are formed at the shortest coupler length of value: $L_c = 3L_\pi/4$ (i.e. $p = 1$ and $q = 4$).

2.3 Imbalances and Excess Losses in Multimode Interference Couplers

Apart from the simplified theory that were presented in the last section, MMI couplers exhibit both imbalances in the fundamental mode power transmitted through the equal-split-ratio output ports and excess losses for the different inputs. The imbalance and excess loss in an MMI coupler is determined by the way the input power from an input excess port is partitioned into the modes exited in the MMI section [16] and the length of the MMI coupler L_c. This partitioning is determined by the relative width W_a/W_{am} and positioning of the access ports of the MMI coupler. Optimization of imbalances and excess losses can be controlled by adjusting the length of the MMI coupler.

In this research, the transmission T_{ij} represents the ratio of the optical power in the fundamental mode transmitted at the access port of output i to the optical power at the access port of input j. Considering an N×N MMI coupler, the access loss L_j due to input j is given by [16]:

$$L_j = -10\log\left(\sum_{i=1}^{N} T_{ij}\right) \tag{2.10}$$

The imbalance $I_{k/l,j}$ in the fundamental mode power of outputs k and l due to input j is given by [16]:

$$I_{k/l,j} = 10\log\left(\frac{T_{kj}}{T_{lj}}\right) \tag{2.11}$$

The imbalance I_{ij} in the transmission T_{ij} for output i might also be defined relative to the mean transmission due to input j as:

$$I_{ij} = 10\log\left(\frac{T_{ij}}{T_{0j}}\right) \tag{2.12}$$

where the mean transmission due to input j, T_{0j}, is given by:

$$T_{0j} = \frac{1}{N}\sum_{i=1}^{N} T_{ij} \tag{2.13}$$

2.4 Optimization of Imbalances and Losses in MMI Couplers

In this section, an objective function for the optimization of imbalances and losses for a N×N MMI coupler is formulated. Let $p_{in,j} = 1$ to represent a unit single mode power exciting the access port of input j of the MMI coupler. The outgoing single mode powers at the output access ports of the MMI coupler for input j are designated as p_{ij}, where $i = 1,2,..,N$. The objective of the minimization of imbalances for input j can be expressed in terms of the minimization of the dimensionless non-uniformity metric ε_j, which represents the difference in the root-mean-square value of the deviations in the outgoing powers p_{ij} from the mean power p_{0j}:

$$\sqrt{\frac{1}{N}\sum_{i=1}^{N}\left(p_{ij} - p_{0j}\right)^2} = \varepsilon_j p_{0j} \tag{2.14}$$

Where the mean power p_{0j} of the outputs for input j is given by:

$$p_{0j} = \frac{1}{N}\sum_{i=1}^{N} p_{ij} \tag{2.15}$$

Dividing both sides of Eq. (2.14) by the unit input power $p_{in,j}$, the non-uniformity metric ε_j can be expressed in terms of the transmissions T_{ij} as:

$$\varepsilon_j = \sqrt{\frac{1}{N}\sum_{i=1}^{N}\left(\frac{T_{ij}}{T_{0j}} - 1\right)^2} \tag{2.16}$$

where T_{0j} is as given by Eq. (2.13). On the other hand, the minimization of the excess losses due to input j can be expressed in terms of the minimization of the power loss metric η_j:

$$p_{in,j} - Np_{0j} = \eta_j p_{in,j} \tag{2.17}$$

Dividing both sides of Eq. (2.14) by the unit input power $p_{in,j}$, the power loss metric η_j can be expressed in terms of the mean transmission T_{0j} as:

$$\eta_j = 1 - NT_{0j} \tag{2.18}$$

The design specification requires:

$$\begin{aligned} \varepsilon_j &\le \varepsilon_0 \\ \eta_j &\le \eta_0 \end{aligned} \tag{2.19}$$

where ε_0 and η_0 are non-uniformity and loss targets. Therefore, an appropriate objective function for the optimization of non-uniformity and loss for input *j* is given by:

$$E_j^2 = \left(\frac{\varepsilon_j}{\varepsilon_0}\right)^2 + \left(\frac{\eta_j}{\eta_0}\right)^2 \tag{2.20}$$

With this choice, the design specification is exceeded if $E^2 < 1$ and missed if $E^2 > 2$. The resultant objective function is convex, non-negative, and zero only if all output powers are equal and sum to the input power. Since the minimum of an objective function is invariant to an overall scaling, one may multiply Eq. (2.20) through by $\varepsilon_0^2\eta_0^2/(\varepsilon_0^2+\eta_0^2)$ to yield:

$$E_j^2 = (1-\sigma^2)\varepsilon_j^2 + \sigma^2\eta_j^2 \tag{2.21}$$

where;

$$\sigma^2 = \frac{\varepsilon_0^2}{\varepsilon_0^2 + \eta_0^2} \tag{2.22}$$

The objective function thus depends upon a design parameter $\sigma \in [0,1]$ that specifies the relative importance of high uniformity ($\sigma \to 0$) relative to low loss ($\sigma \to 1$). The same non-uniformity and loss performance is required irrespective of the choice of the input port. Therefore, a total objective function for the minimization of non-uniformities and losses for the different inputs of the N×N MMI coupler might be given by:

$$E^2 = \frac{1}{N}\sum_{j=1}^{N} E_j^2 = (1-\sigma^2)\varepsilon^2 + \sigma^2\eta^2 \tag{2.23}$$

where;

$$\varepsilon^2 = \frac{1}{N}\sum_{j=1}^{N}\varepsilon_j^2, \qquad \eta^2 = \frac{1}{N}\sum_{j=1}^{N}\eta_j^2 \tag{2.24}$$

2.5 Design of Multimode Interference Couplers

The design of the different MMI couplers used in the IPPAS fabrics is presented. The silicon core thickness of the used template is 300 nm. The design of the MMI couplers is carried at an operating wavelength of $\lambda = 1550$ nm. The complex FDM-3D-FV solver of the simulation tool FIMMPROP is used in design. The single mode transmissions, imbalances, excess losses and optimization objective functions are all extracted from accurate simulation data. All of the MMI couplers are designed to meet or exceed the previously reported typical performance parameters. Simulations of the power intensity distribution inside the designed MMI couplers are also included. The scattering parameters of the designed MMI couplers, as functions of wavelength, are extracted from simulation results and used to determine the broadband response of the deigned IPPAS elements.

2.5.1 Design of a -3dB 2×2 SOI-MMI Coupler

In this section the design of a -3dB 2×2 MMI coupler having the geometry shown in Figure 2.1 is presented. The maximum width allocated for each access port is set to $W_{am} = 2$ μm yielding a coupler width of $W_c = 4$ μm. The same value of W_{am} is used for the other 4×4 and 8×8 MMI couplers designed in this work to yield the same pitch size of 2 μm between the centers of the I/O access ports no matter what combination of MMI couplers is used in any IPPAS fabric. A -3dB split ratio (50:50%) is obtained around the coupler length $L_c = 3L_\pi/2$.

To find an appropriate value for the access port width, the simulated imbalance and excess loss is scanned versus W_a within the available range from W_g to W_{am}-$2W_f$ for the designed -3dB MMI coupler. Figure 2.2 depicts this simulation around the optimum access port width of about $W_a = 1.49$ μm. This value of the access port width is used in the design of the other 4×4 and 8×8 MMI couplers presented in this work providing the observation that imbalance is guided by the W_a/W_{am} ratio.

Scan of the simulated imbalance and excess loss versus the length of the coupler L_c is depicted in Figure 2.3. The design of the coupler length is set at the point of minimum excess loss. At the coupler length of $L_c = 60.66$ µm, the imbalance is $I_{1/2,1} = 0.053$ dB and the excess loss is $L_1 = 0.11$ dB based on simulation. The simulated optical power distribution inside the designed -3dB 2×2 MMI coupler due to input I_1 is shown in Figure 2.4.

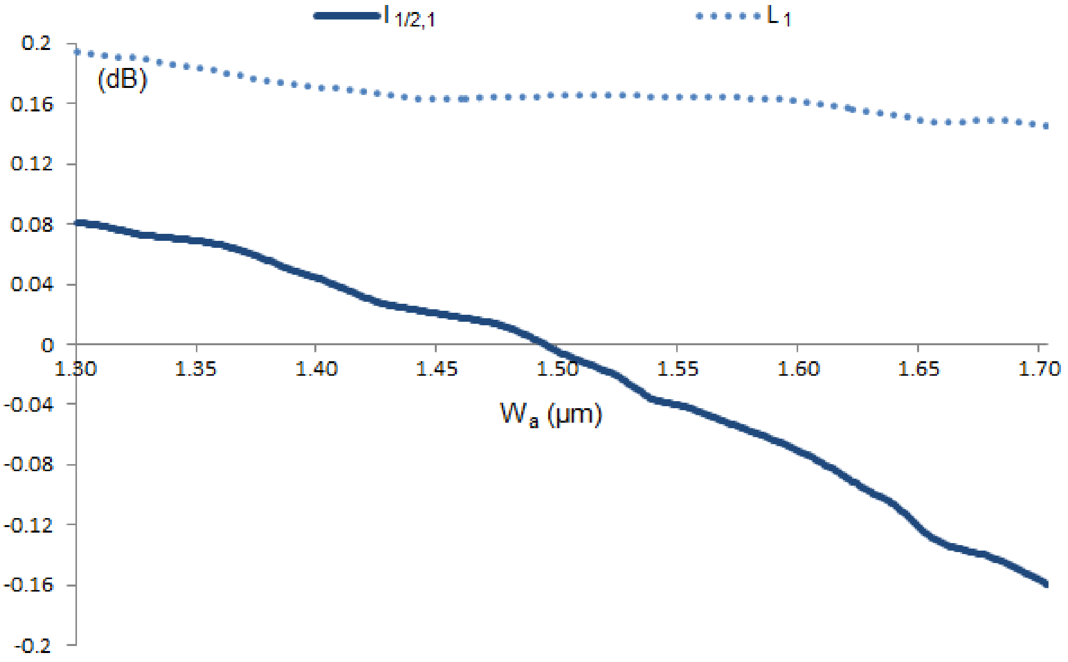

Figure 2.2 Simulation of the imbalance and excess loss versus the access port width for the -3dB 2×2 MMI coupler.

2.5.2 Design of a Crossover 2×2 SOI-MMI Coupler

An ideal crossover 2×2 MMI coupler produces 0dB of relative power at the output access port located at the side opposite to the input access port. The length of a crossover 2×2 MMI coupler is around $L_c = 3L_\pi$; i.e. about twice the length of a -3dB 2×2 MMI coupler having the same width. The geometry of the crossover 2×2 MMI coupler designed in this work is shown in Figure 2.5.

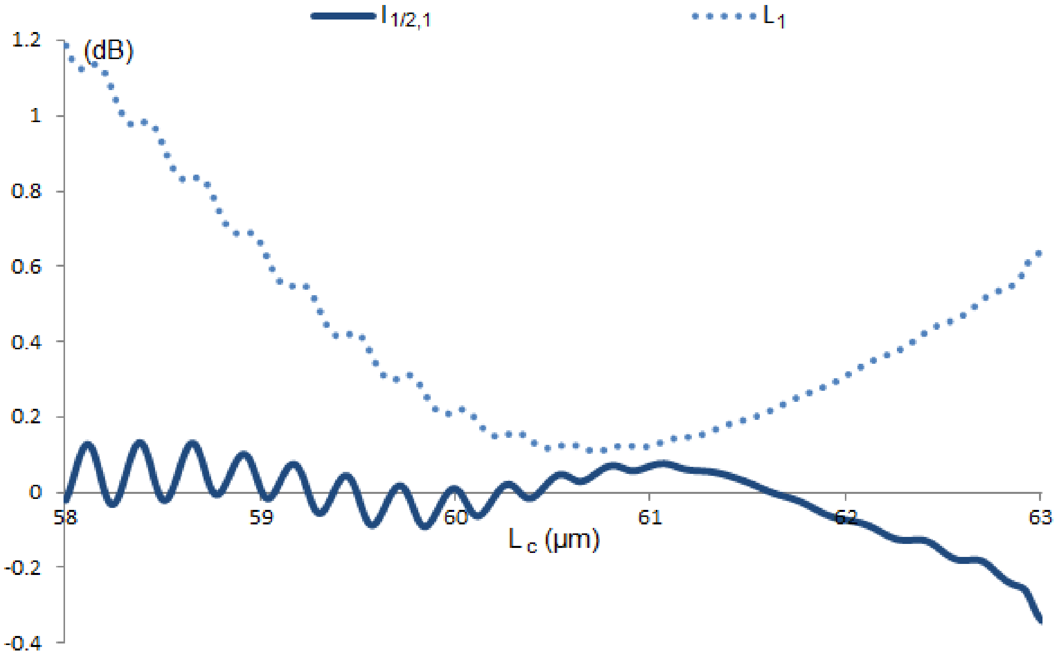

Figure 2.3 Simulation of the imbalance and excess loss versus the coupler length for the -3dB 2×2 MMI coupler.

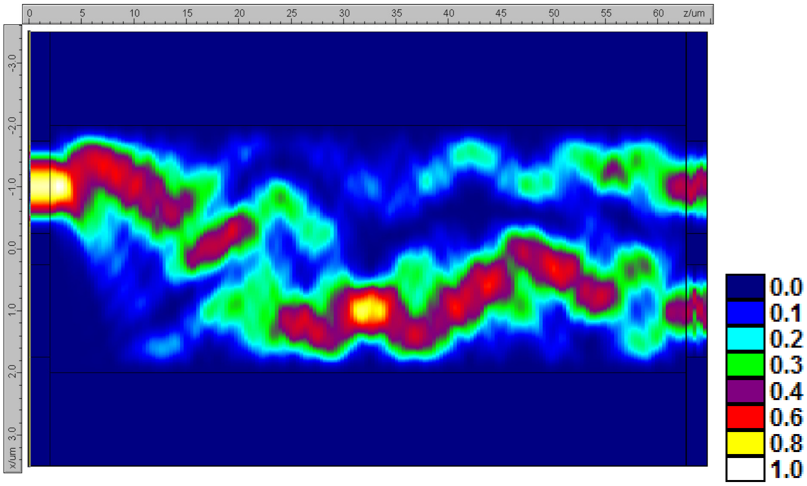

Figure 2.4 Simulated optical power distribution inside the designed -3dB 2×2 MMI coupler of Figure 2.1.

The access port width is set to the same value used for the -3dB 2×2 MMI coupler, $W_a = 1.49$ µm, and the same pitch size of 2 µm separates the centers of the adjacent I/O access ports in order to have the designed crossover 2×2 MMI coupler native to the IPPAS fabrics. Therefore, the crossover 2×2 MMI coupler has a width of $W_c = 3.49$ µm.

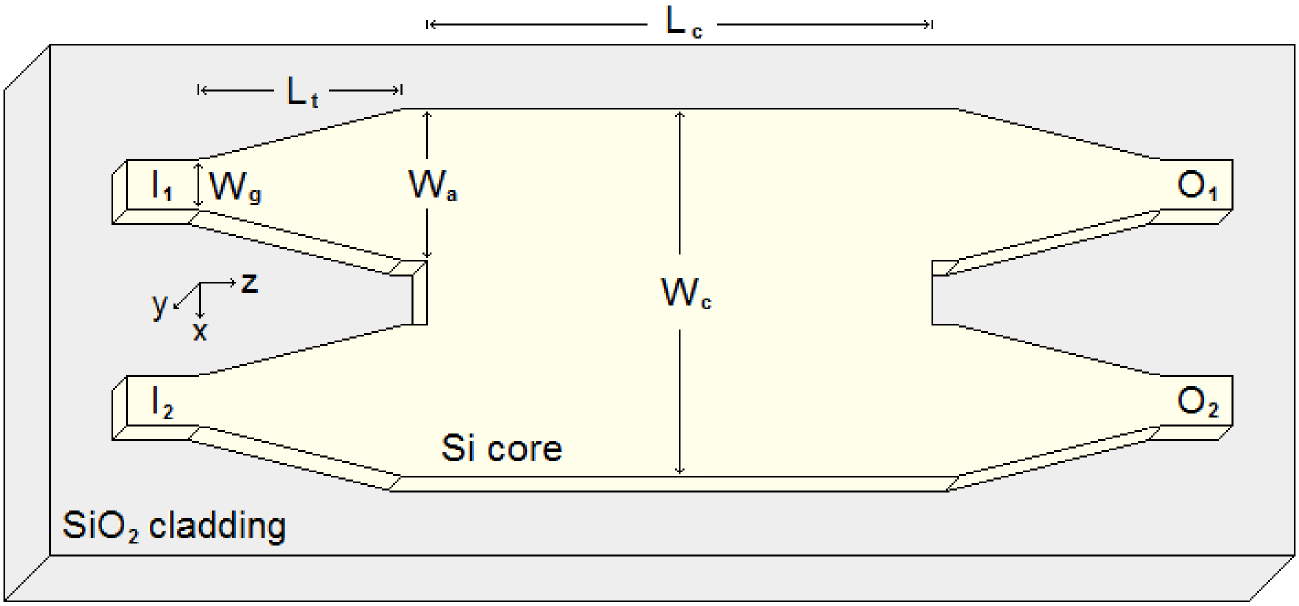

Figure 2.5 Geometry of a crossover 2×2 MMI coupler.

The simulated transmissions and excess loss versus the coupler length for the designed crossover 2×2 MMI coupler are shown in Figure 2.6. A minimum excess loss of only 0.122 dB is obtained at the coupler length $L_c = 94.55$ µm based on simulation. The crosstalk at the design point is -31.9 dB based on simulation. The simulated optical power distribution inside the designed crossover 2×2 MMI coupler due to input I_1 is shown in Figure 2.7.

2.5.3 Design of a -6dB 4×4 SOI-MMI Coupler

An ideal -6dB 4×4 MMI coupler produces an equal -6dB of relative power at each output due to any one of the applied inputs. The geometry of the designed -6dB 4×4 MMI coupler is shown in Figure

2.8; seemed to be an extension for the geometry of the -3dB MMI coupler of Figure 2.1. Each access port of width W_a is centered at the W_{am} allocated maximum access port width. Again, W_{am} is set to 2 µm yielding $W_c = 8$ µm of coupler width. The access port width is set to the value of $W_a = 1.49$ µm as indicated before. A -6dB 4×4 MMI coupler is localized at around the coupler length $L_c = 3L_\pi/4$.

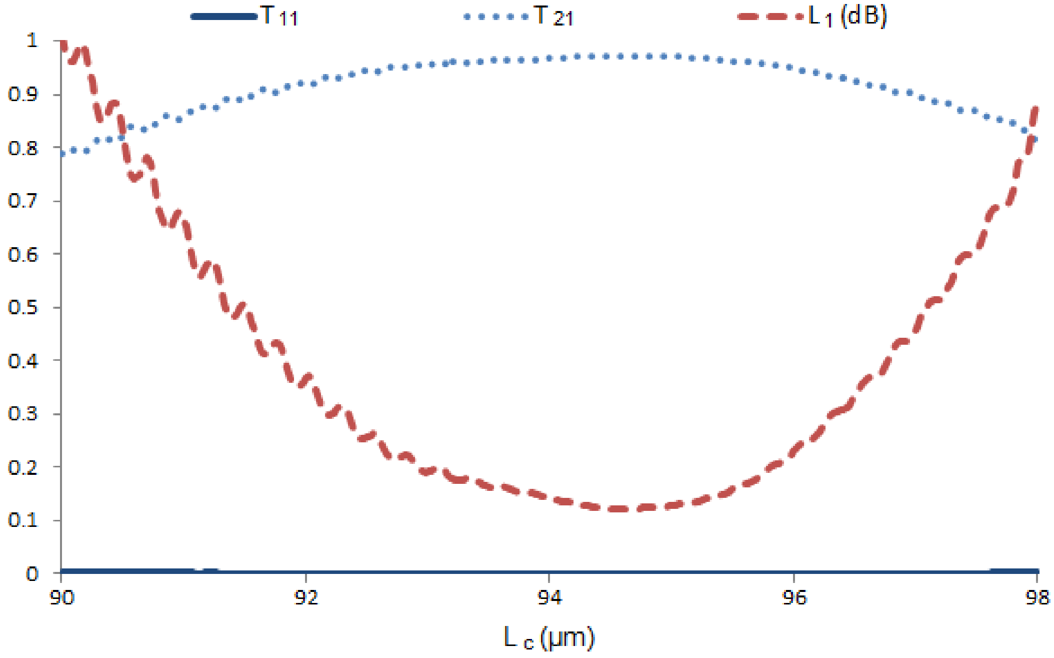

Figure 2.6 Simulation of the transmissions and excess loss versus the length of the crossover 2×2 MMI coupler.

Taking both inputs I_1 and I_3 into consideration, the imbalances $I_{1/4,1}$, $I_{2/3,1}$, $I_{1/4,3}$ and $I_{2/3,3}$ and excess losses L_1 and L_3 are simulated in Figure 2.9 versus the coupler length. The simulation of the optimization function E for the minimization of both non-uniformity ε and loss η is depicted in Figure 2.10. The optimum MMI coupler length for the minimization of non-uniformity and loss is $L_c = 122.094$ µm and $L_c = 122.281$ µm, respectively. The two coupler length values are close from each other. The design coupler length is set at $L_c = 122.2$ µm. The designed 4×4 MMI coupler has a maximum imbalance of 0.074 dB and maximum excess loss of 0.377 dB based on simulation. The simulated optical power distribution inside the designed -6dB 4×4 MMI coupler due to both inputs I_1 and I_3 are shown in Figure 2.11.

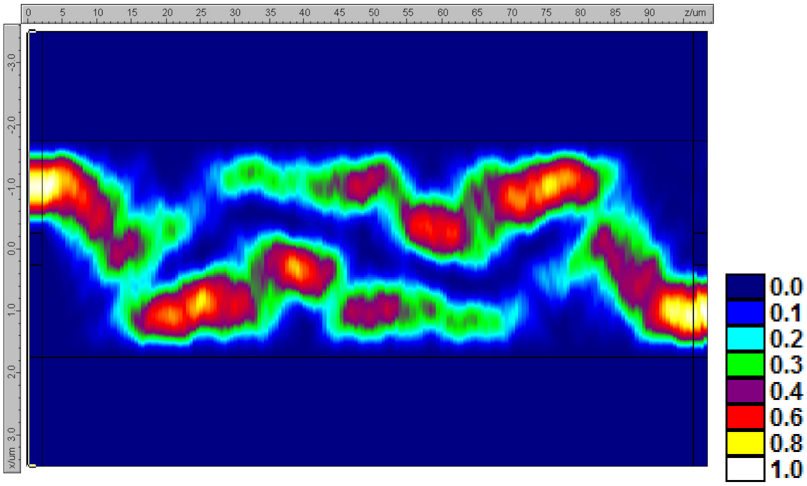

Figure 2.7 Simulated optical power distribution inside the designed crossover 2×2 MMI coupler of Figure 2.5.

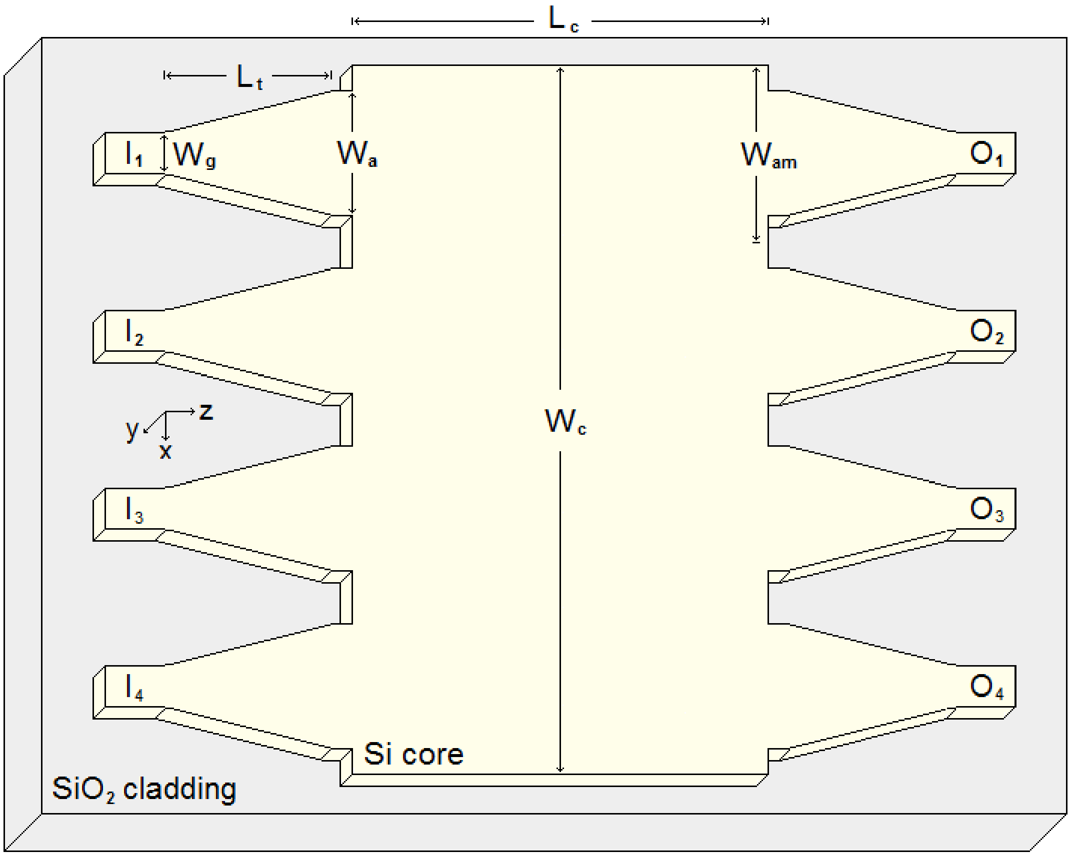

Figure 2.8 Geometry of a -6dB 4×4 MMI coupler.

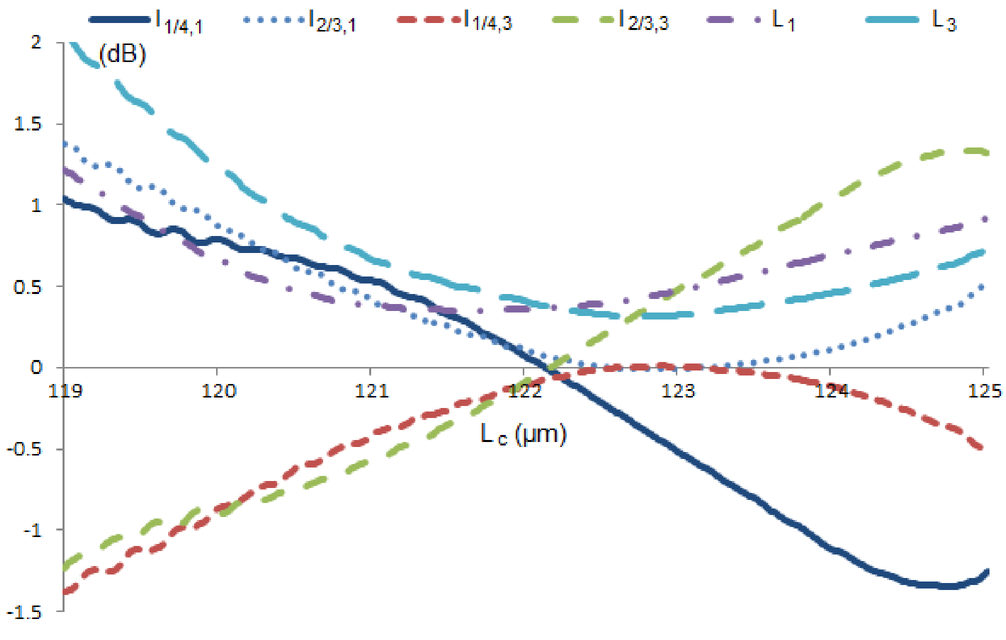

Figure 2.9 Simulation of the imbalances and excess losses versus the length of the -6dB 4×4 MMI coupler.

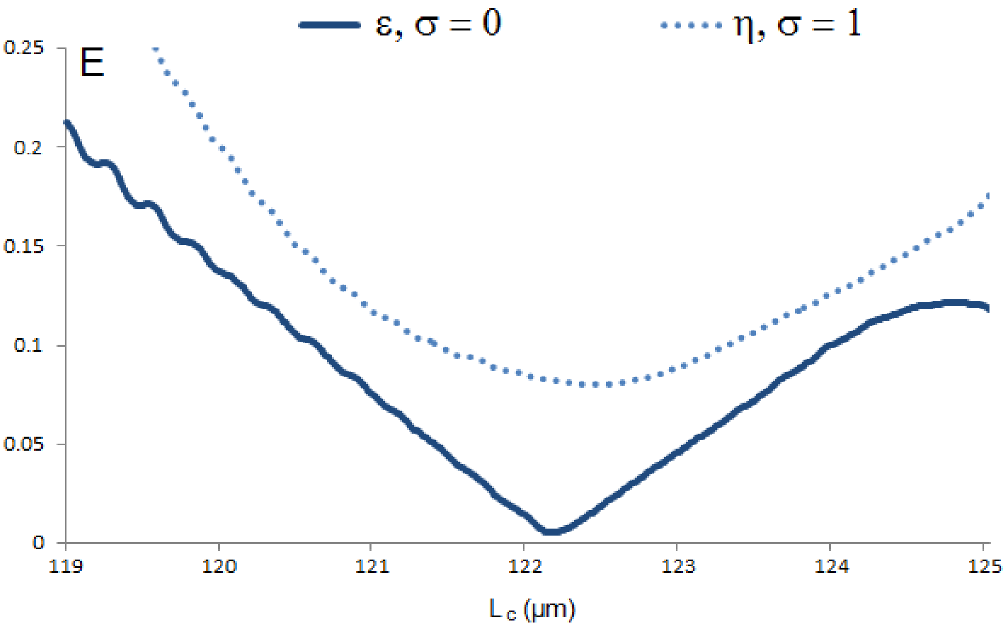

Figure 2.10 Simulation of the optimization function versus the length of the -6dB 4×4 MMI coupler.

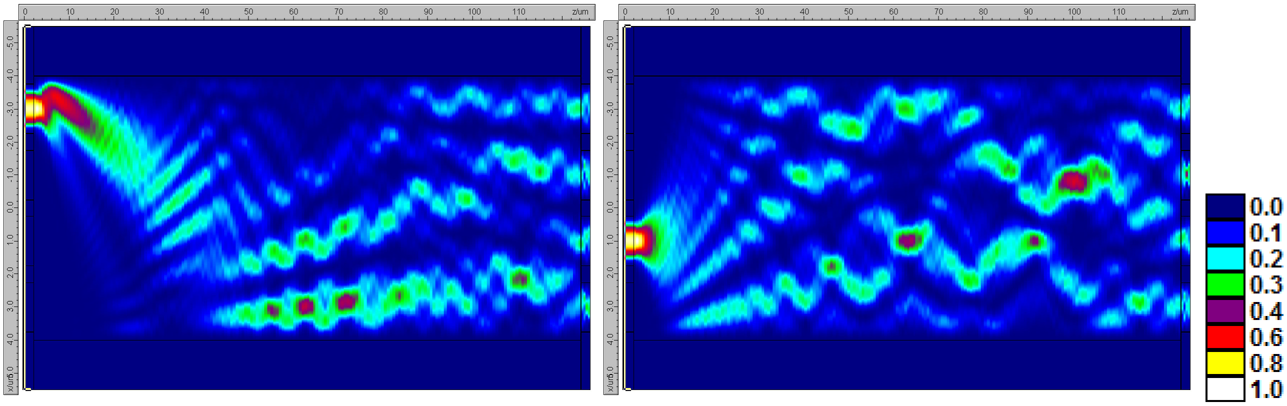

Figure 2.11 Simulated optical power distribution inside the designed -6dB 4×4 MMI coupler of Figure 2.8. Inputs I_1 and I_3 are applied in the left and right side figures, respectively.

2.5.4 Design of a -3dB 4×4 SOI-MMI Coupler

A -3dB 4×4 MMI coupler is designed around the coupler length $L_c = 3L_\pi/2$. An ideal -3dB 4×4 MMI coupler produces -3dB of relative power at each of outputs O_1 and O_4 when applying the input to either I_1 or I_4 and produces also -3dB of relative power at each of outputs O_2 and O_3 when applying the input to either I_2 or I_3. The geometry of the -3dB 4×4 MMI coupler is the same as that in Figure 2.8 for the -6dB 4×4 MMI coupler but with about double the coupler length.

The access port and coupler widths are set as before; $W_a = 1.49$ µm and $W_c = 8$ µm, respectively. Simulation of the imbalances $I_{1/4,1}$ and $I_{2/3,3}$ and excess losses L_1 and L_3 when applying the inputs to I_1 and I_3, respectively, are depicted in Figure 2.12. The minimization of the non-uniformity ε and loss η objective functions is simulated in Figure 2.13. The MMI coupler lengths for optimized non-uniformity and optimized loss are 243.457 µm and 246.68 µm, respectively. The difference in the two coupler lengths for optimized non-uniformity and optimized loss is much larger than it was for the case of the -9dB 4×4 MMI coupler.

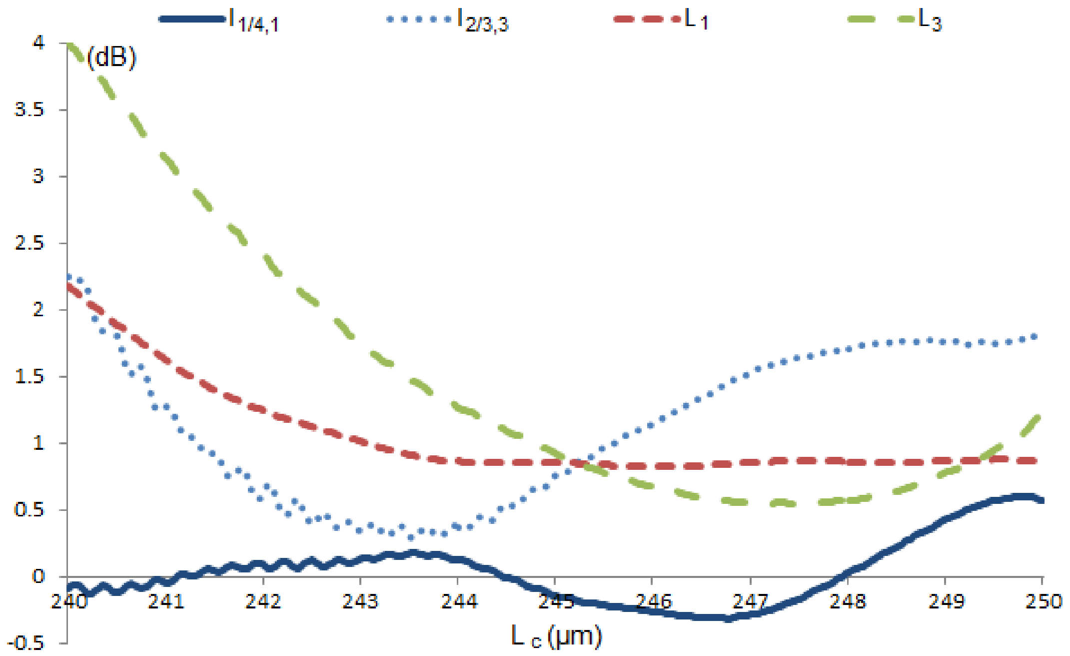

Figure 2.12 Simulation of the excess losses versus the length of the -3dB 4×4 MMI coupler.

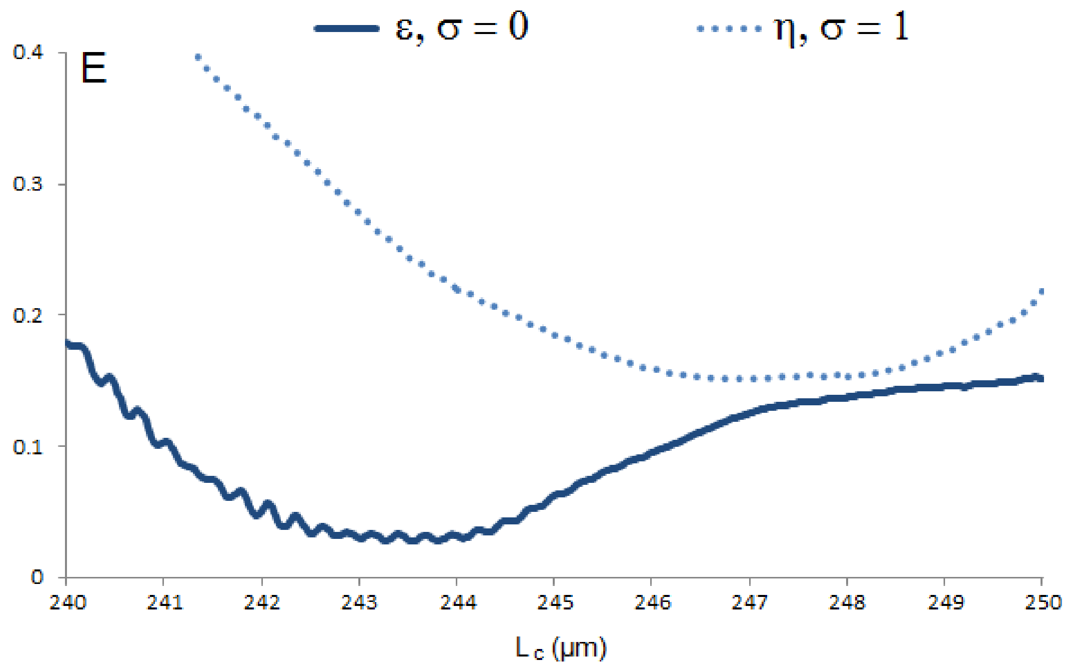

Figure 2.13 Simulation of the optimization function versus the length of the -3dB 4×4 MMI coupler.

The design length of the -3dB 4×4 MMI coupler is set at $L_c = 243.46$ µm close to the point of minimized imbalances. The designed -3dB 4×4 MMI coupler has maximum values of imbalance, loss and crosstalk of 0.285 dB, 1.47 dB and -28.87 dB, respectively, based on simulation. The simulated optical power distribution inside the designed -3dB 4×4 MMI coupler due to both inputs I_1 and I_3 are shown in Figure 2.14.

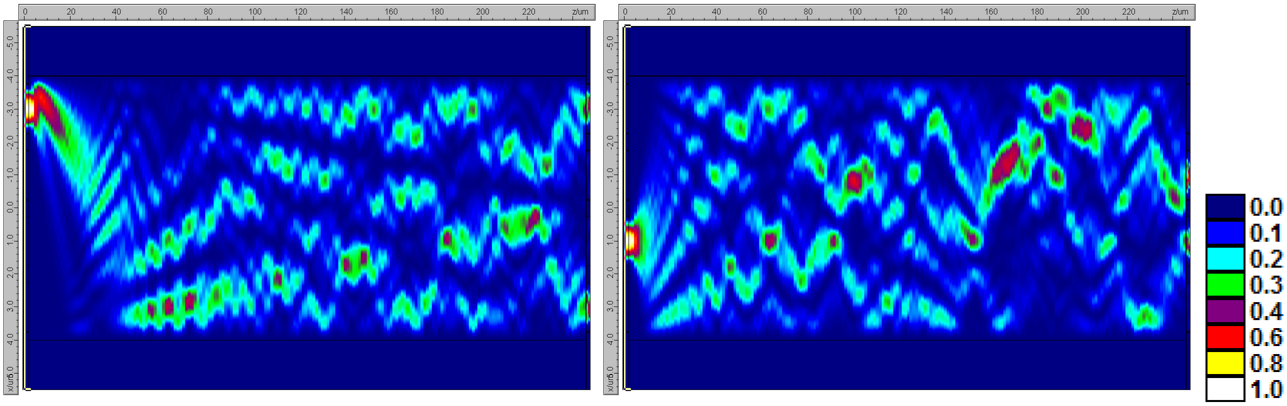

Figure 2.14 Simulated optical power distribution inside the designed -3dB 4×4 MMI coupler of Figure 2.8. Inputs I_1 and I_3 are applied in the left and right side figures, respectively.

2.5.5 Design of a -9dB 8×8 SOI-MMI Coupler

An ideal -9dB 8×8 MMI coupler produces an equal -9dB of relative power at each output due to any one of the applied inputs. Imbalances and excess losses increase with the increase in the number of inputs and outputs making the design of the -9dB 8×8 MMI coupler more challenging. The geometry of the -9dB 8×8 MMI coupler is similar to that of a -6dB 4×4 MMI coupler with the difference of having eight inputs and eight outputs.

The same width parameters of $W_a = 1.49$ µm and $W_{am} = 2$ µm are used in the design of the -9dB 8×8 MMI coupler yielding a coupler width of $W_c = 16$ µm. The simulated excess losses for inputs I_1, I_3, I_5 and I_7 are depicted in Figure 2.15.

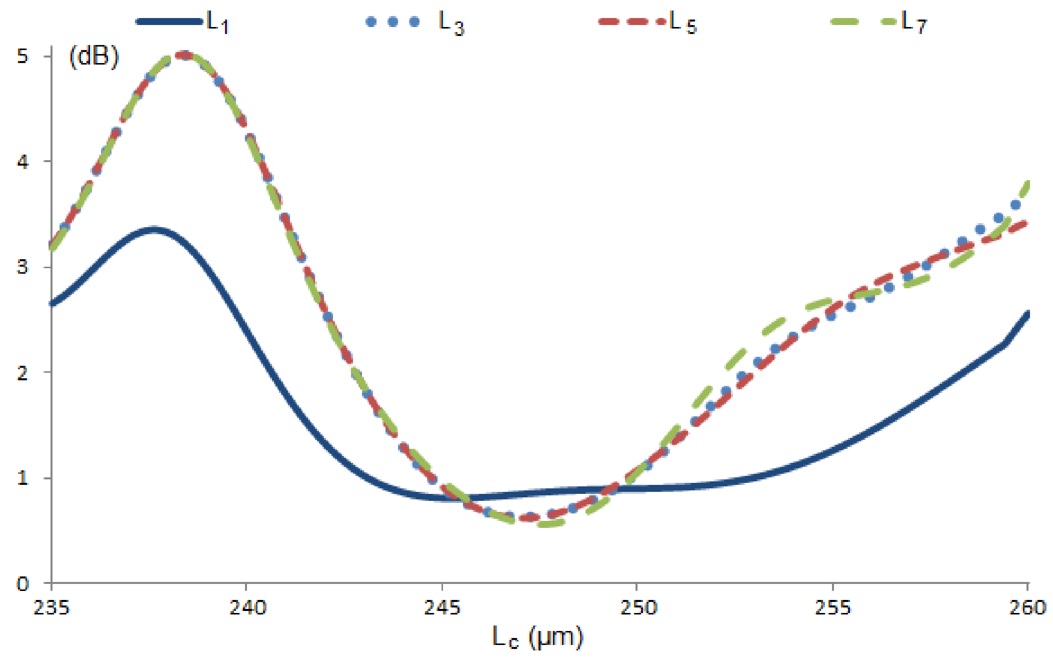

Figure 2.15 Simulation of the excess losses versus the length of the -9dB 8×8 MMI coupler.

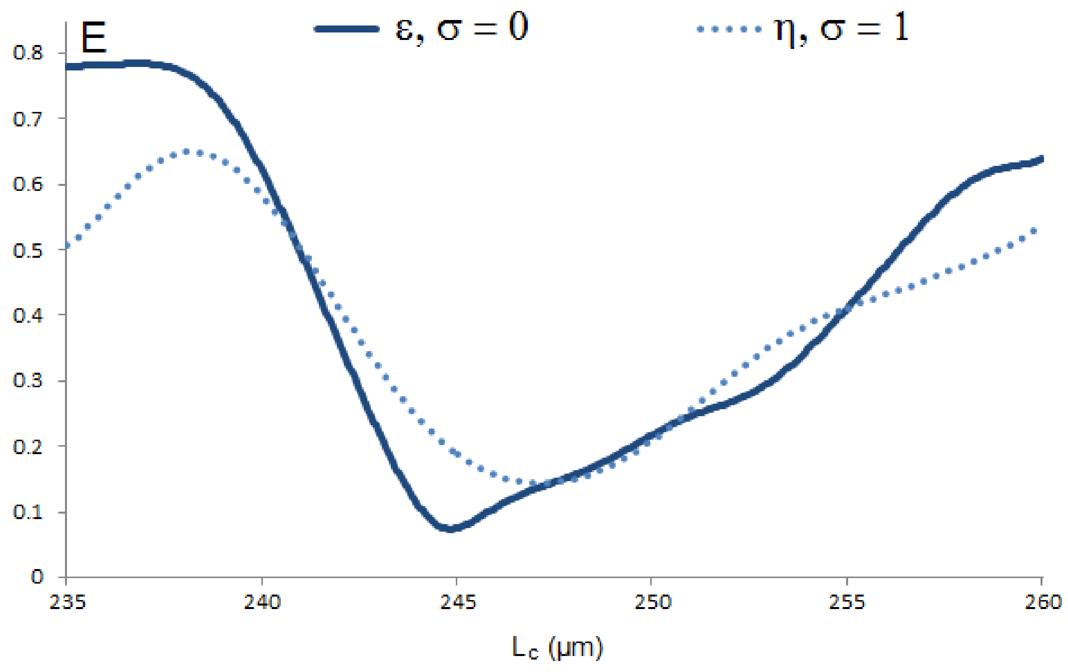

Figure 2.16 Simulation of the optimization function versus the length of the -9dB 8×8 MMI coupler.

The minimization of the non-uniformity ε and loss η objective functions is simulated in Figure 2.16. The -9dB 8×8 MMI coupler lengths for optimized non-uniformity and optimized loss are 244.57 µm and 246.816 µm, respectively. The designed -9dB 8×8 MMI coupler length is set to $L_c = 245.7$ µm. Based on simulation, the maximum imbalance is 1.73 dB and the maximum excess loss is 0.82 dB at the design point. The simulated optical power distribution inside the designed -9dB 8×8 MMI coupler due to inputs I_1, I_3, I_5 and I_7 are shown in Figure 2.17.

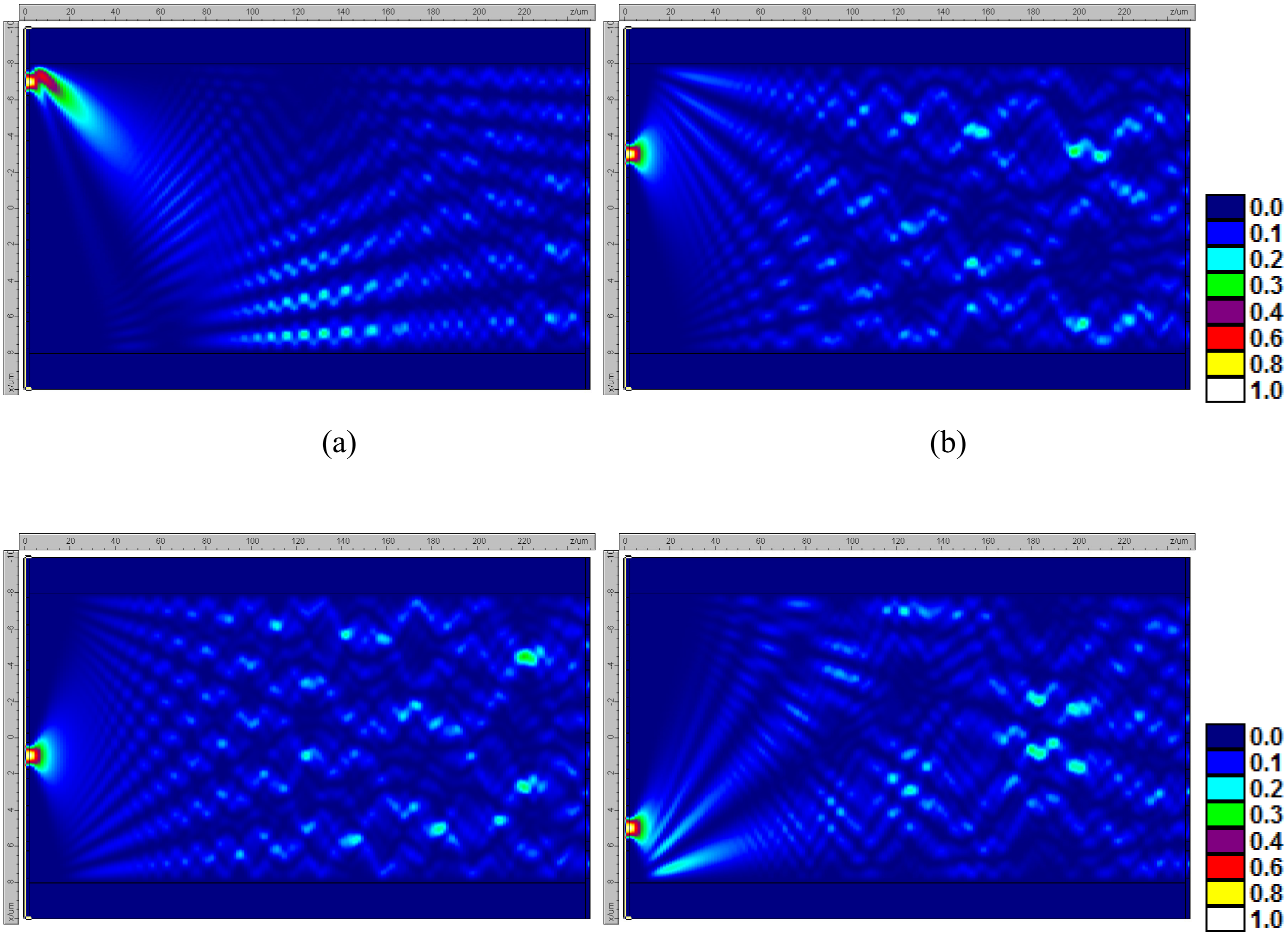

(a) (b)

(c) (d)

Figure 2.17 Simulated optical power distribution inside the designed -9dB 8×8 MMI coupler. Inputs I_1, I_3, I_5 and I_7 are applied in (a) through (d), respectively.

2.6 Design of a Taper Adapter for the SOI-MMI Couplers

The design, behavior and testing of adiabatic and near-adiabatic tapered sections with simple and complex geometries have been investigated in literature, e.g. [21-23]. In this research, a conventional linear-geometry taper long enough to persist near adiabatic behavior is adopted for simplicity. The conventional linear taper is used to adapt the width of the interconnecting single mode nanowires, $W_g = 350$ nm, to the width of the I/O access ports of the different MMI couplers used in the IPPAS elements, $W_a=1.49$ µm. The simulation of the excess loss versus the length of the taper is depicted in Figure 2.18. It seemed to be that a taper length of about 10 µm is proficient. In the transition region of the taper lengths, $L_t << 10$ µm, multimode interference is resulted and radiation modes cause more excess loss. The 10 µm is a saturated near-adiabatic taper length used in IPPAS elements. The simulated optical power distribution inside the designed conventional linear taper of 10 µm length is depicted in Figure 2.19.

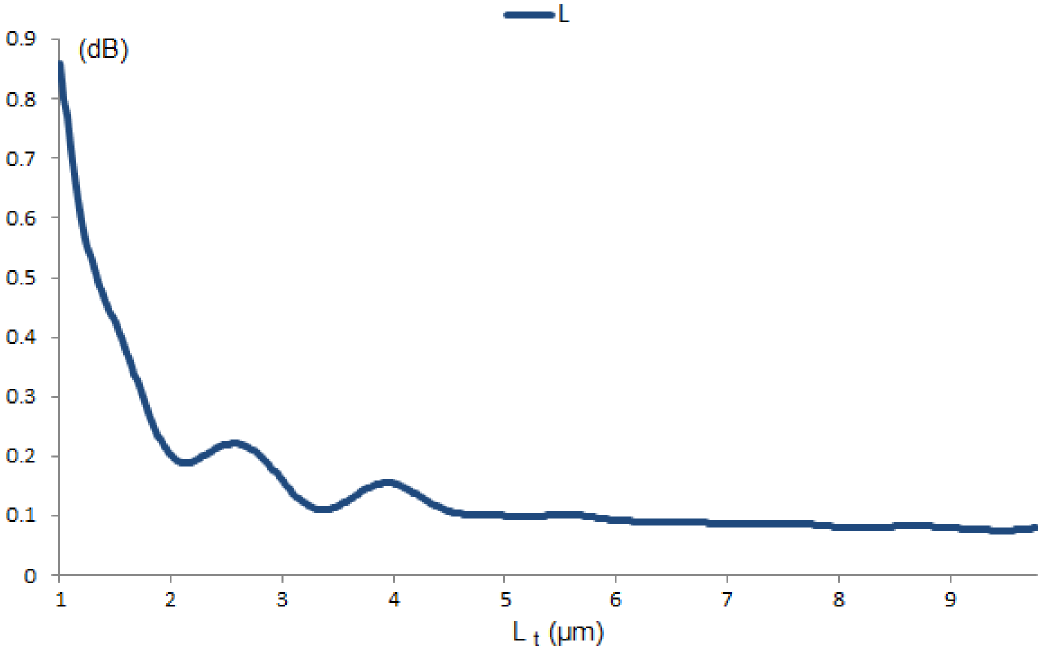

Figure 2.18 Simulation of the excess losses versus the length of the taper adapter.

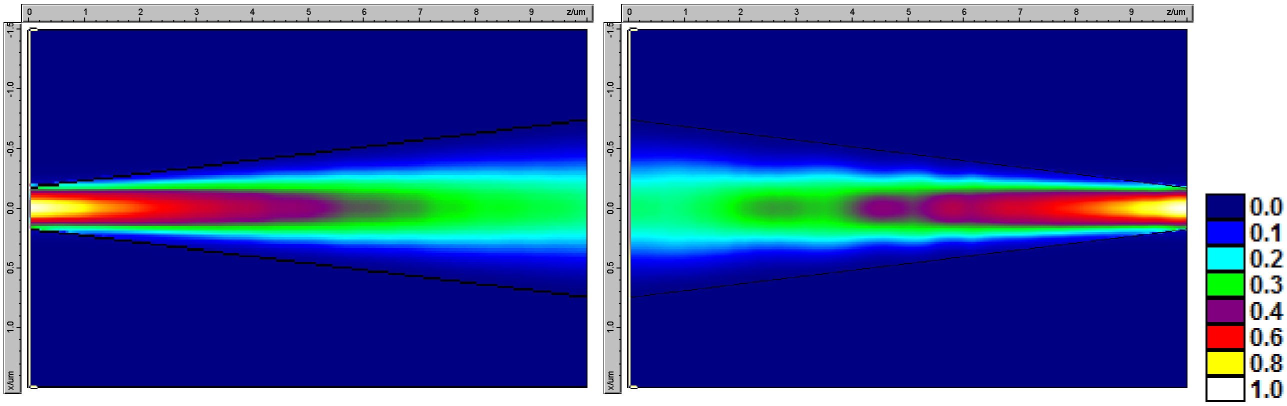

Figure 2.19 Simulated optical power distribution inside the taper of 10 μm length. *Left:* a taper at an input access port. *Right:* a taper at an output access port.

CHAPTER 3

ANALYSIS, DESIGN AND SIMULATION OF NANO-ELECTROMECHANICAL PHASE SHIFT ELEMENTS AND RESPONSE OF PHASED ARRAY SWITCHES

3.1 Abstract

In this chapter, the structure and principle of operation of the NEMS-operated under-etched slot waveguide acting as a phase shift element is illustrated. The behavior of the under-etched slot waveguide is described in terms of numerical analysis utilizing the simulation of the effective index of the under-etched slot waveguide as a function of its voltage-modulated slot width. The results of simulation and numerical analysis are used in the design of a 180º capable phase shifter composed of 15 cascaded under-etched slot waveguides. The structure and simulation of the designed transition slot couplers used to couple the interconnecting waveguides to the slotted phase shift lines is also presented. The transmission-phase response of some IPPAS elements of sizes 2×2 and 4×4 to some phase synthesis profiles applied to their phase shifters is examined.

3.2 Structure and Analysis of the under-Etched Slot Waveguide

In this research, the development of the NEMS-operated phase shifters is based on the NanoSOI nanomachining fabrication process offered by CMC Microsystems; by utilizing their Soitech wafer with the option of 300 nm thickness of silicon base layer on the buried oxide of 1 µm thickness. The resist is patterned using e-beam lithography achieving small feature size in the order of 100 nm. Both metal patterning and etching under the silicon base layer in the buried oxide has made it possible to support developing the active voltage-controlled phase shifters using the Soitech platform. The wavelength of operation is set to $\lambda = 1550$ nm in the design procedure.

The NEMS-operated phase shift element uses suspended slotted photonic waveguides with an electrostatically controlled variable slot width. The slotted photonic wire in essence consists of two nanoscale silicon beams with sub-micron separation (100 nm) that are rendered free to move laterally relative to each other by using an under-etch step in the fabrication process to remove the oxide layer underneath the silicon beams.

The use of a single under-etched slot waveguide and latter a line of cascaded under-etched slot waveguides were already introduced by Acoleyen et al. in [1,24]. The structure and dimensions of the under-etched slot waveguide used in this research is explained in Figure 3.1. It consists of two suspended silicon beams each of width W_{gs} (230 nm) and height h (300 nm) equals the thickness of the silicon base layer of the SOI wafer. The length of the under-etched slot is L_s. The slot width between the suspended silicon beams at standstill, i.e. when no potential difference is applied between the silicon beams, is W_{s0} (100 nm). An applied voltage difference modulates the slot width between the suspended silicon beams to W_s as a function of the propagation distance along the under-etched slot. Alternatively, the excursion width W_{ex} is described as:

$$W_{ex} = \frac{W_{so} - W_s}{2} \tag{3.1}$$

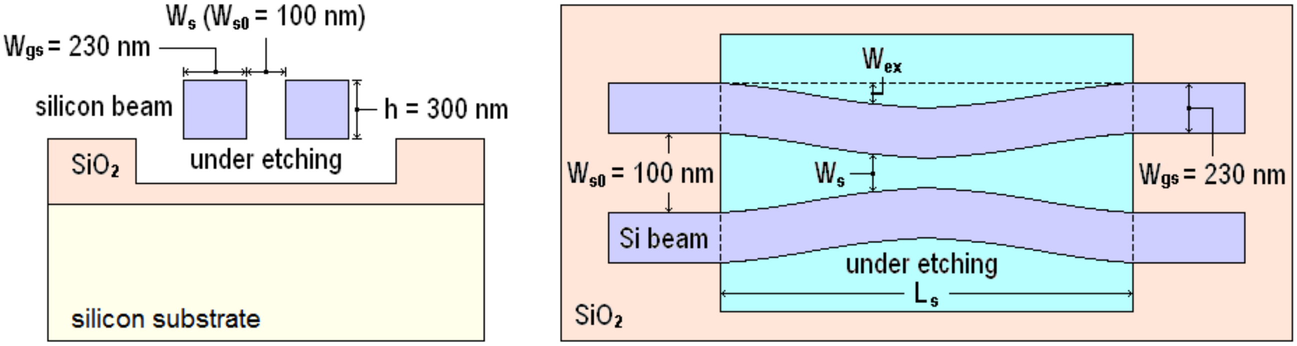

Figure 3.1 Geometry of the under-etched slot waveguide.

Electrically, the two silicon beams of the under-etched slot waveguide behave as a charged capacitor when applying voltage difference to it causing the suspended beams to be attracted to each other, modulating the slot width in the process. This results in large modulation in the effective index based on which principle the phase shifter works. At the pull-in voltage the two suspended beams of the under-etched slot waveguide becomes in direct contact with each other at the midpoint. This causes the electromechanical system to become unstable and can cause collapse of the under-etched slot waveguide.

The positive z-axis is taken here as the direction of propagation. The phase difference $\Delta\phi$ introduced due to modulating the slot width of the NEMS-operated slot waveguide is given by:

$$\Delta\phi = \frac{2\pi}{\lambda}\left[\int_0^{L_s} n_e dz - n_{e0} L_s\right] \tag{3.2}$$

In Eq. (3.2), the effective index n_e is a function of the slot width W_s which by itself is a function of the propagation distance z; i.e. $n_e(z) = n_e[W_s(z)]$. The term $(2\pi/\lambda)n_{e0}L_s$ in Eq. (3.2) corresponds to the phase without applying voltage to the under-etched slot waveguide. Therefore, n_{e0} represents the effective index when the slot width equals to W_{s0}; i.e. $n_{e0} = n_e(W_{s0})$. The dependency on W_s and z is removed from Eq. (3.2) for simplicity. The wavelength λ is taken here as the free-space wavelength.

When applying voltage to the silicon beams, the excursion of the beams due to the capacitive attraction lateral forces can be described by the Euler-Bernoulli beam equation, which provides a mean for calculating small deflections in beams due to applied distributed load. The axial stress is neglected in the formulation. Further relating the distributed load to the capacitive attraction distributed force between the silicon beams as in [1] reveals the following nonlinear forth-order differential equation that describes the beams excursion:

$$\frac{d^4 W_{ex}}{dz^4} = \frac{\varepsilon_o h V^2}{2EI\left(W_{s0} - 2W_{ex}\right)^2} \tag{3.3}$$

V is the voltage applied across the slot between the two suspended silicon beams. E is Young's modulus and is equal to 169 GPa in the core silicon at the direction of interest. The beam's area moment of inertia in the direction of interest is given in terms of the beam's width and thickness as in [1] by:

$$I = \frac{hW_{gs}^3}{12} \tag{3.4}$$

The solution of Eq. (3.3) is achieved numerically subjected to fixed and hinged boundary conditions. Fixed boundary conditions allow no displacement and no rotation at the clamping points:

$$W_{ex} = 0, \quad \frac{dW_{ex}}{dz} = 0 \quad at \quad z = 0, L_s \tag{3.5}$$

Hinged boundary conditions allow no displacement, but do allow rotation around the clamping points:

$$W_{ex} = 0, \quad \frac{d^2W_{ex}}{dz^2} = 0 \quad at \quad z = 0, L_s \tag{3.6}$$

The simulation of the effective index as a function of the slot width and the numerical solution of Eq. (3.3) allows the determination of the phase difference achieved by the voltage activated suspended silicon beams of the under-etched slot waveguide based on Eq. (3.2).

The speed of the nanomechanical suspended silicon beams of the under-etched slot waveguide depends on their mechanical relaxation time. The expected speed is in the MHz range. The fundamental resonance frequency of the nanomechanical structure is given in [1] by:

$$f_o = \frac{K^2}{2\pi L_s^2}\sqrt{\frac{EI}{\rho h W_{gs}}} \tag{3.7}$$

ρ = 2.329 g.cm^{-3} is the silicon mass density. The factor K equals to 4.73 for fixed boundary conditions and equals to π for hinged boundary conditions. The other significant factor affecting the speed of the NEMS-operated phase shifter is the distributed RC circuit of the feeding arrangements from the electrodes to the phase shift line. The distributed capacitance of the structure is mainly formed due to three contributions: the voltage-dependent capacitances of the suspended silicon beams of the cascaded under-etched slot waveguide sections, the fixed-value capacitances of the slot waveguide support segments between the cascaded under-etched slot waveguide sections and the fixed-value capacitances of the transition slot couplers used to couple the phase shift line to the interconnecting single mode waveguides while providing voltage bias to the phase shift line of cascaded NEMS-operated slot waveguide sections. The overall capacitance of the NEMS-operated phase shifter designed in this work is estimated to be in the femto Farad range (around 10 fF). The RC lowpass filtering limit affecting the speed of the system might be relieved in the manufacturing process if the doping level of the silicon core of the used wafer is made high enough to reduce the overall resistance between the electrodes and the NEMS-operated phase shift line such that the only factor affecting the speed would be due to the frequency of resonance of the nanomechanical suspended silicon beams. Examining the RC speed limiting factor versus the nanomechanical frequency of resonance would be made possible when testing the fabrication variants of the designed NEMS-operated phase shifter.

3.3 Design of the NEMS-operated Phase Shifter

The design of the NEMS-operated slot waveguide phase shifter is based on the numerical approach presented by Acoleyen et al. [1], which was explained in the last section (3.2), and the simulation of the effective index of the slot nanowire using FIMMPROP. Acoleyen designed, fabricated and tested a NEMS-operated phase shifting line of three cascade under-etched slot waveguides that could achieve up to about 40º of phase shit difference. Examining the testing results of Acoleyen, it seemed to be that the electromechanical behavior of the NEMS-operated slot nanowire is located (about midway) between fixed and hinged boundary conditions of the freestanding silicon beams. Here, a similar procedure is followed to design a single under-etched slot waveguide based on the Soitech wafer with the 300 nm of silicon thickness option. Then, 15 freestanding slot waveguides are cascaded to form a 180° phase shift line coupled through high efficiency transition slot waveguides.

The simulations of the designed full NEMS-operated phase shifter as well as the transition slot couplers are displayed here.

The width of each one of the freestanding silicon beams (W_{gs} = 230 nm) and the slot width (W_{s0} = 100 nm) are selected to support propagating the fundamental mode in the under-etched slot waveguide. The simulation of the effective index n_e of the under-etched slot waveguide for the fundamental mode is depicted as a function of the modulated slot width in Figure 3.2. Here, a minimum slot width $W_{s,min}$ of 20 nm is allowed as a guard before the applied pull-in voltage causes the two silicon beams to come in direct electrical contact with each other at the midpoint along the under-etched slot length.

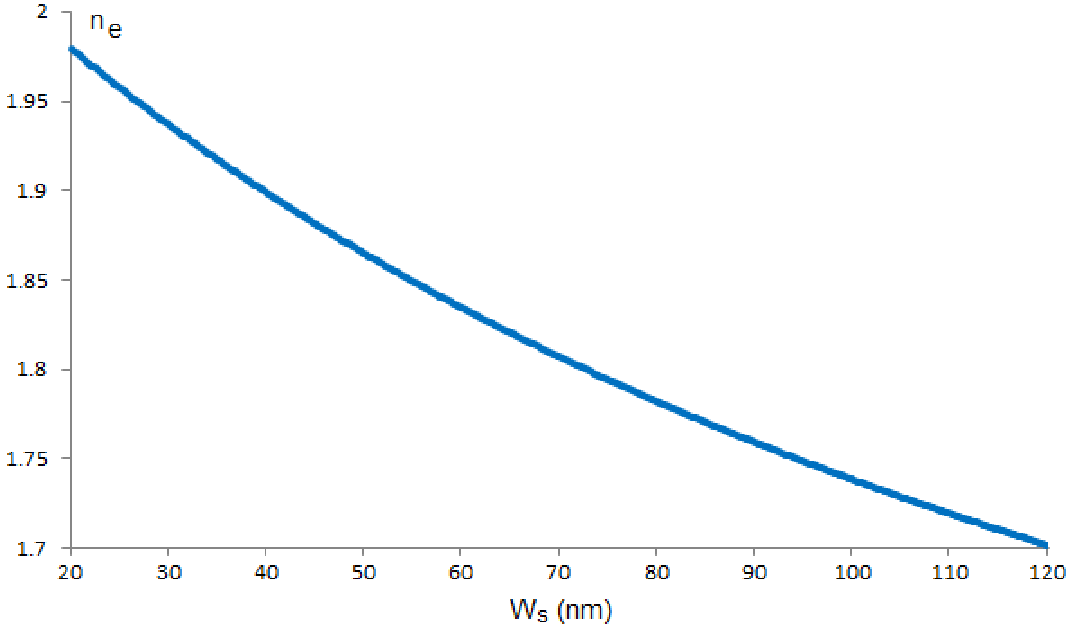

Figure 3.2 Simulation of the effective index for the fundamental mode of the under-etched slot waveguide versus the slot width.

Utilizing the data of the modulated effective index of Figure 3.2 and equations (3.1) through (3.6), the predicted phase difference as a function of the length of the NEMS-operated slot waveguide, for an operating voltage of 15 V applied to the suspended silicon beams, is shown in Figure 3.3. From this Figure, the length of the under-etched slot waveguide is selected as 5.4 µm. Each under-etched slot waveguide at this length might achieve up to an average phase shift between fixed and hinged boundary conditions of about 16.6°. Therefore, at least about 11 cascaded under-etched slot waveguides are needed to achieve up to 180° of phase shift at an operating voltage of 15 V. However, we put a fairly large margin in our consideration by constructing a relatively long phase shift line of 15 cascaded under-etched slot waveguides.

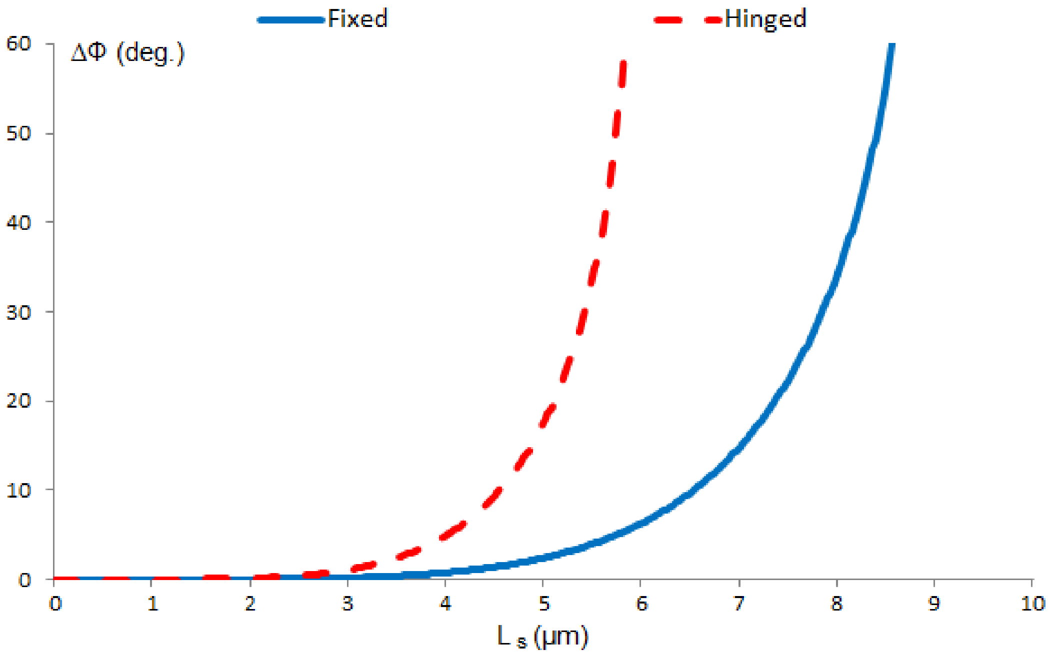

Figure 3.3 Predicted phase difference versus the length of the NEMS-operated slot waveguide for an operating voltage of 15 V.

The phase shift characteristic of a single under-etched slot waveguide, at the design length L_s = 5.4 µm, as a function of the voltage applied to the silicon beams for both fixed and hinged boundary conditions is depicted in Figure 3.4. From this figure we find that the possible pull-in voltage at hinged boundary conditions (worst case premise) is about 17.7 V.

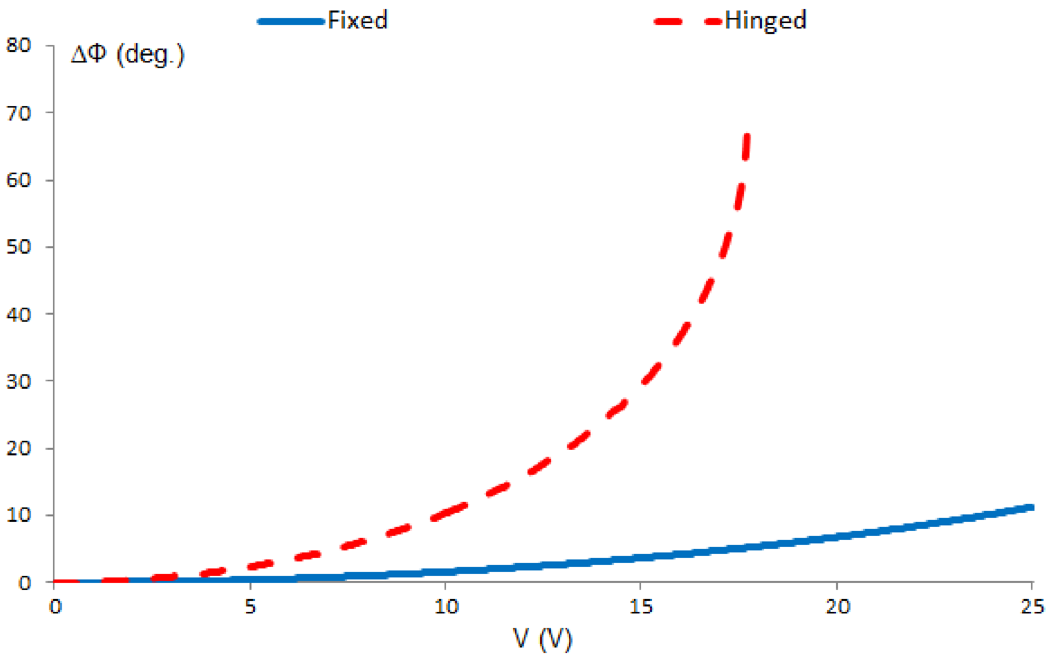

Figure 3.4 Predicted phase difference versus the voltage applied to a NEMS-operated slot waveguide of length L_s = 5.4 µm.

The fundamental resonance frequency of the nanomechanical suspended silicon beams as a function of the length of the under-etched slot waveguide is displayed in Figure 3.5. At the design length of the under-etched slot waveguide of 5.4 µm, the fundamental resonance frequency is about 50 MHz. Increasing the fundamental resonance frequency of the suspended silicon beams is possible by decreasing the length of the under-etched slot waveguide. However, a smaller length yields less phase shift capability of each cascaded under-etched slot waveguide that requires increasing the number of the cascaded under-etched slot waveguides, which in consequence results in increasing the excess loss of the NEMS-operated phase shifter. The design, therefore, is a tradeoff between speed, based on the resonance frequency of the suspended silicon beams, and loss.

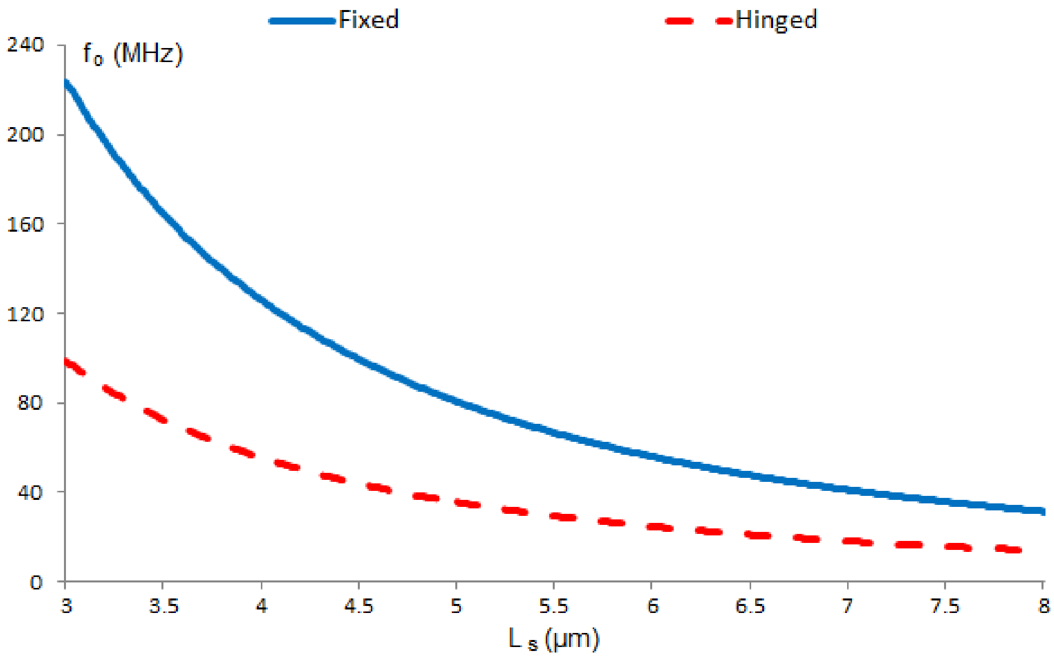

Figure 3.5 Fundamental resonance frequency versus the under-etched slot waveguide length.

The schematic diagram of the designed phase shift line of 15 cascaded free standing slot waveguides with the I/O straight transition slot couplers is shown in Figure 3.6. The designed NEMS-operated phase shifter is just 349 µm in overall length entitling it as the most compact phase shifter compared to its Thermo-optic effect, carrier dispersion effect or electro-optic effect counterparts.

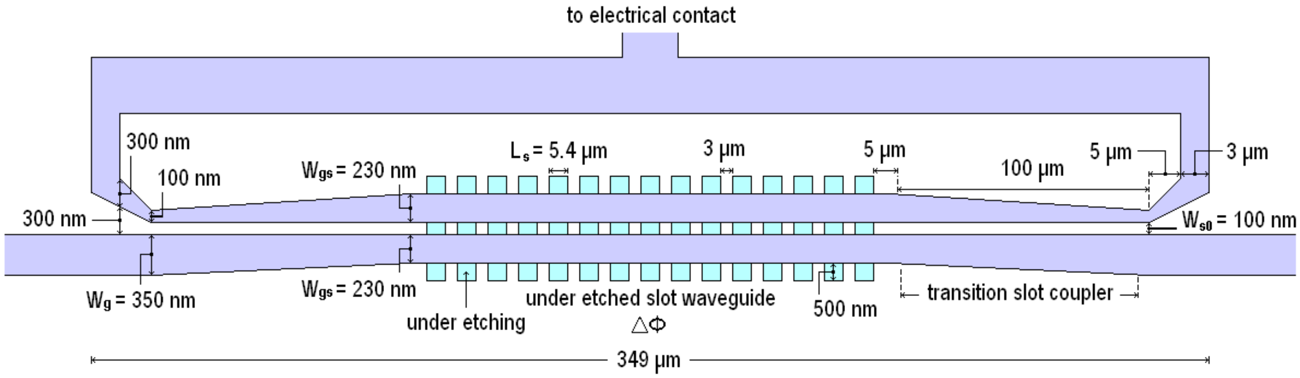

Figure 3.6 Schematic diagram of the NEMS-operated phase shifter of 15 cascaded under-etched slot waveguides with the transition slot couplers and voltage feeding arrangements.

Simulations of the optical power distribution inside the designed NEMS-operated phase shifter and transition slot couplers, at an operating wavelength of $\lambda = 1550$ nm, are depicted in Figure 3.7. Based on simulation statistics, the designed phase shifter introduces a total excess loss of about 1.1 dB, and each additional under-etched slot adds an excess loss of about 0.055 dB. For the design transition slot coupler length of 100 μm, the optical mode coupling efficiency of each transition slot coupler is about 97% based on simulation.

3.4 Response of Photonic Phased Array Switch Elements

The applications of the photonic phased array switch elements depend on the thorough understanding of the response of them. Whether used in photonic signal routing, modulation and demodulation of the optical carrier, coherent detection or optical signal processing, the response of an IPPAS element is concerned with the determination of transmission-phase relations of its outputs related to its inputs taking the phases applied through the NEMS-operated phase shifters of the IPPAS element as driving parameters. Different modes of operation are available to any of the IPPAS elements introduced in this research depending on the phase synthesis profile applied to the active phase shifters. In essence, the phase shifters can control both the intensity and phase of the optical carrier at one of the outputs of an IPPAS element due to an input in a desired way. Some simple operational mode phase synthesis profiles are demonstrated in this section.

Considering the 2×2 phased array switch element of Figure 1.3, the differential imbalanced phase synthesis profile is defined by:

$$\Delta\phi = \begin{cases} \Delta\phi_1 & when \quad 0^o < \Delta\phi < 180^o \\ -\Delta\phi_2 & when \quad -180^o < \Delta\phi < 0^o \end{cases} \tag{3.8}$$

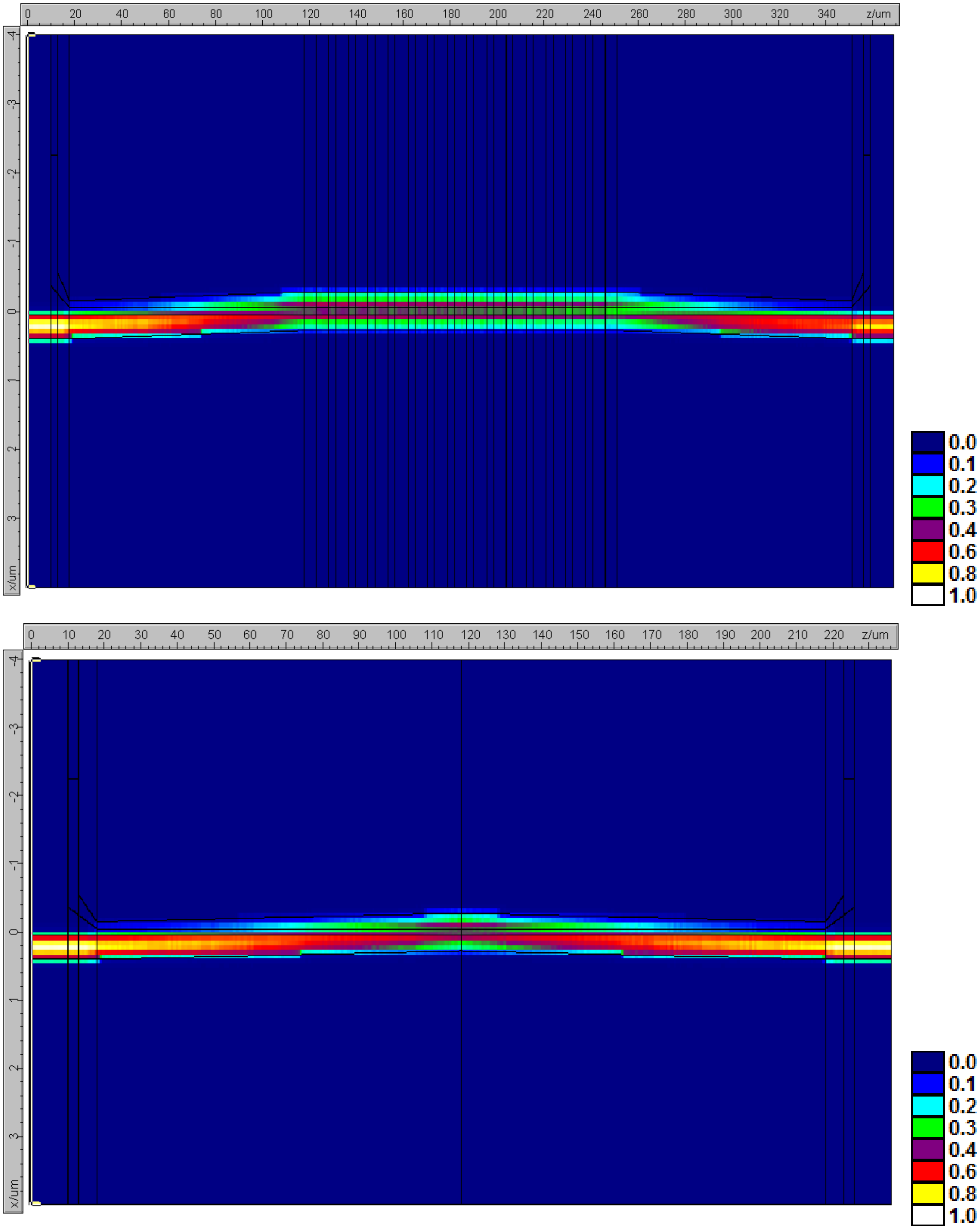

Figure 3.7 Optical power distribution inside the designed NEMS-operated phase shifter (up) and a directly connected I/O transition slot couplers (down).

$\Delta\phi_1$ and $\Delta\phi_2$ are the phase shift differences applied through the two phase shifters of the switch element. It is also possible to express the phase difference $\Delta\phi$ in this case as: $\Delta\phi = \Delta\phi_1 - \Delta\phi_2$, providing that $\Delta\phi_2 = 0^o$ when $\Delta\phi > 0^o$, and that $\Delta\phi_1 = 0^o$ when $\Delta\phi < 0^o$. This means one phase shifter is activated by applying voltage to it at one time while keeping the other phase shifter at reset condition. The transmission and phase responses of outputs O_1 and O_2 of the 2×2 IPPAS element of Figure 1.3 for both inputs I_1 and I_2 based on the phase synthesis profile described by Eq. (3.8) are depicted in Figure 3.8.

The phase information of the optical carriers at the outputs of the 2×2 IPPAS element illustrated in Figure 3.8 is interpreted as relative to each other. The relative phase information of all the optical carriers at the outputs can be rotated by any arbitrary amount of phase shift equivalent to propagating all of the outputs through waveguides having the same arbitrary length.

When $\Delta\phi = 0^o$, input I_1 is directed to output O_2, and input I_2 is directed to output O_1. The aforementioned output states are reversed when applying $\Delta\phi = \pm 180^o$. The relative phase relations between the output states are also altered for the different settings of $\Delta\phi$. This behavior of the 2×2 IPPAS element in the differential imbalanced phase synthesis profile regime is proper for applications like switching and binary Phase-Shift-Keying (BPSK) modulation. For the in-between values of $\Delta\phi$, i.e. rather than 0 and ±180°, the optical carrier at each one of the two outputs is changing both its intensity and phase information simultaneously. Therefore, a distinct analog control of the intensity or phase of the optical carrier requires a different phase synthesis profile regime. The study of the phase synthesis profile regimes is being investigated utilizing constellation space response diagrams.

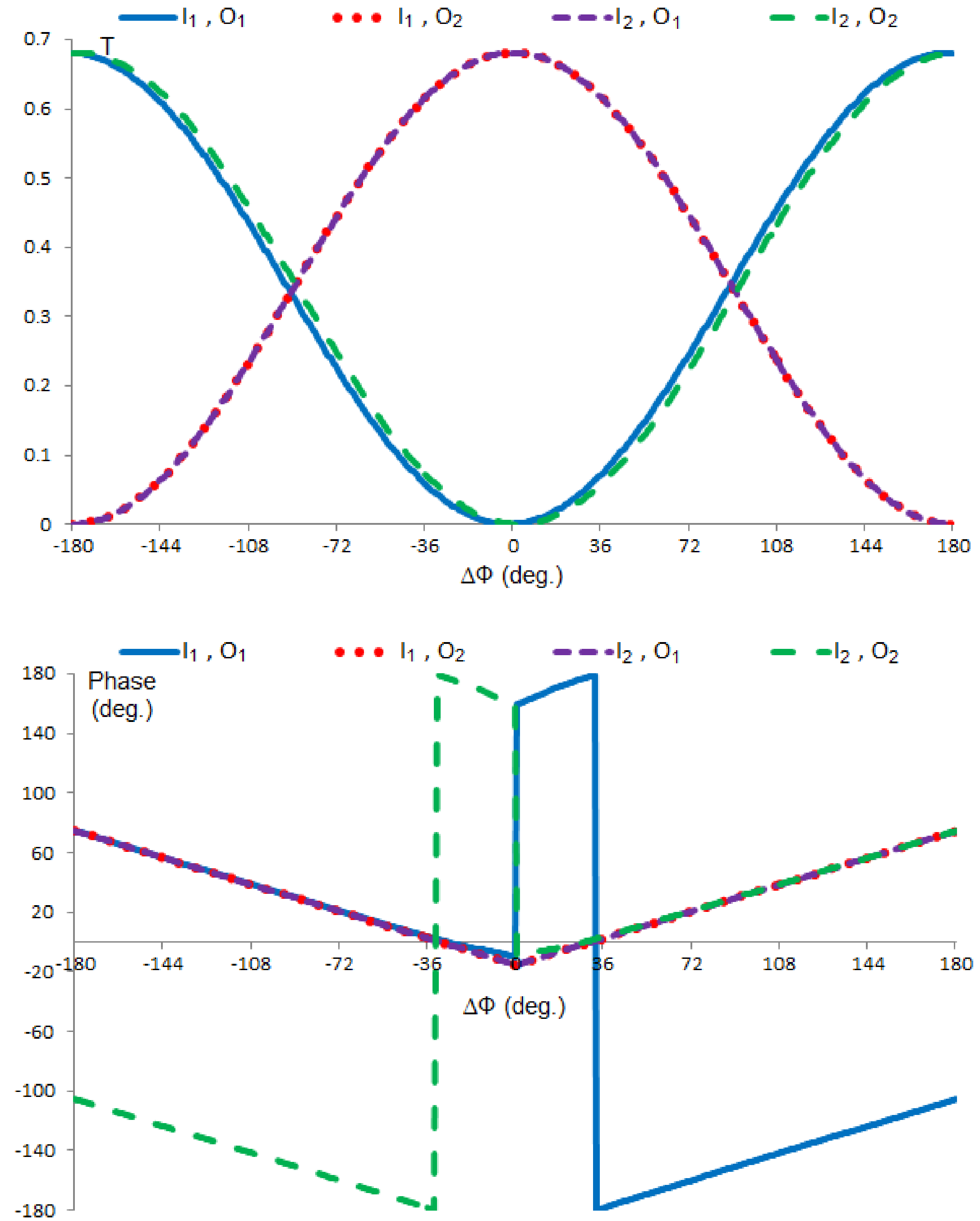

Figure 3.8 Simulation of transmission (up) and relative phase (down) for the 2×2 IPPAS element of Figure 1.3 in response to a differential imbalance phase synthesis profile.

The broadband response of any of the designed IPPAS elements requires the determination of the wavelength response of the MMI couplers. The wavelength responses of the different designed MMI couplers have been simulated and used in custom code programs to determine the response of the IPPAS elements. Figure 3.9 depicts the broadband transmission wavelength response of the 4×4 IPPAS element of Figure 1.6 when distinctively routing each of inputs I_1 and I_3 to outputs O_2 and O_4, respectively.

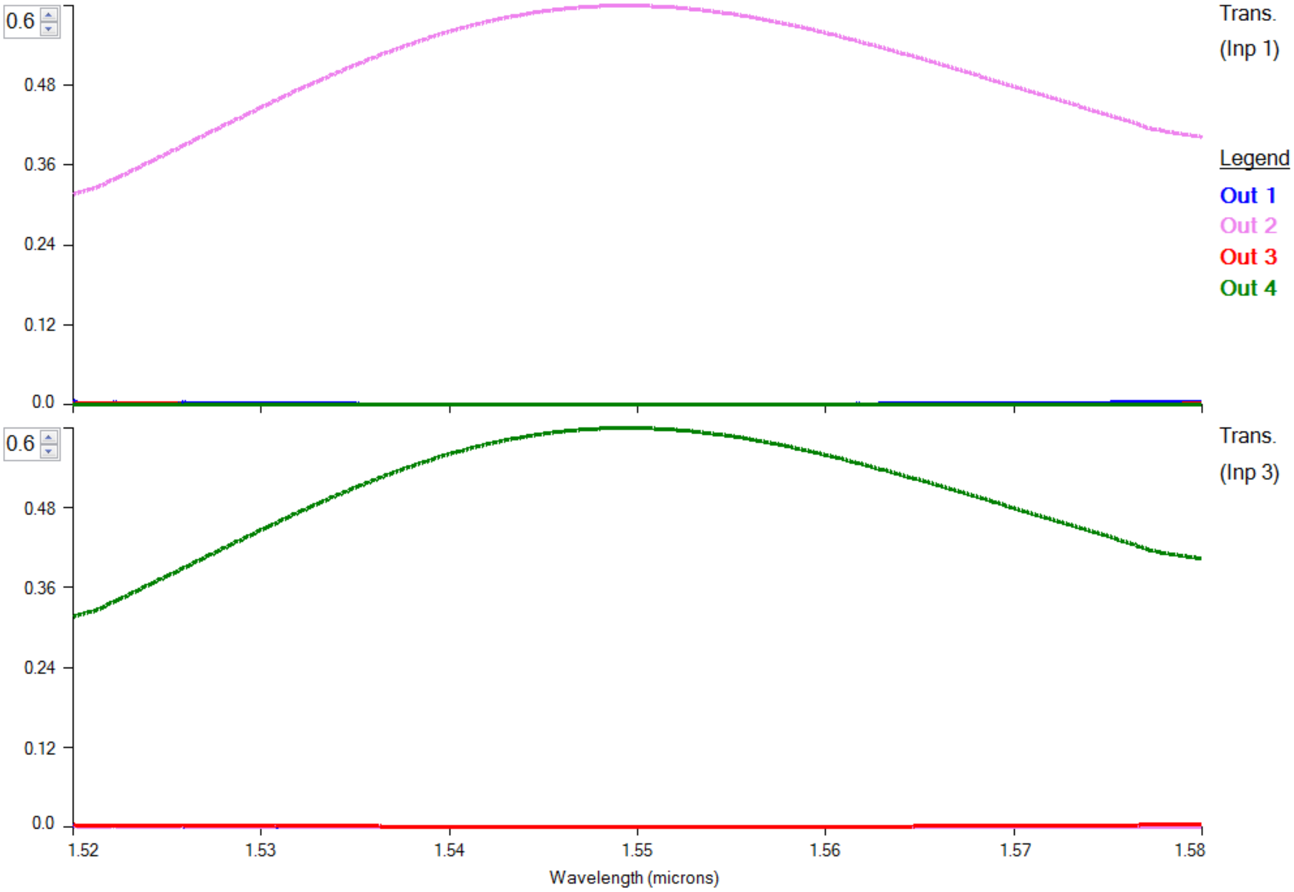

Figure 3.9 Simulation of transmission versus wavelength for the 4×4 IPPAS element of Figure 1.6. *Up:* Input I_1 is routed to output O_2. *Down:* input I_3 is routed to output O_4.

CHAPTER 4

GENERAL REMARKS, CONCLUSIONS AND FUTURE WORK

The investigation presented in this thesis has been devoted to the design and simulation of novel integrated photonic phased array switches having multiple numbers of I/O ports ranging from 2×2 to 8×8. Each IPPAS element presented in this thesis is composed of a number of NEMS-operated active phase shifting branches interconnecting a splitter and combiner MMI couplers. When the number of interconnecting phase shifters are more than two, crossover MMI couplers are used to bring the inner interconnecting branches to the exterior sides to enable the placement of the phase shifters at the sides of the switch element; examples are the 4×4, 4×8 and 8×8 IPPAS elements presented in chapter 1. Each phase shifter is biased from one side facing to the exterior side of the switch element facilitating placing the electrodes around the switch element. Simulations using the complex FDM-3D-FV solver of the simulation tool FIMMPROP and numerical analysis are deployed to design the components of the phased array switch elements to typical parameters.

Chapter 1 of this thesis mainly presents the topologies of the designed IPPAS elements. The switch elements are based on a SOI platform having silicon core thickness of 300 nm. The oxide layer beneath the silicon core is under-etched at specific locations to utilize the fabrication of nano-electromechanical components. Details of the dimensions of the components of the designed IPPAS elements are indicated on the schematic diagrams introduced in this chapter. The NEMS-operated phase shifter is just 349 µm in length, which is the smallest reported length compared to its counterparts found in contemporary literature. The designed phase shifter utilizes 15 cascaded sections of under-etched slot waveguides allowing producing up to 180º phase shift at an operating voltage of up to about 15 V. The length of the designed IPPAS elements, excluding the I/O coupling parts, is ranging from 528.32 µm for the 2×2 IPPAS element to 2331 µm for the 8×8 IPPAS element. The chapter also reflects the fact that IPPAS elements are candidates in a number of applications including modulation, detection, signal processing and conditioning, switching and wavelength division multiplexing.

The analysis of MMI couplers is presented in chapter 2. The eigen modes propagation in the multimode region of the MMI coupler is formulated based on a simplified theory. Imbalances and excess losses are defined and used as performance parameters for the design of MMI couplers of different sizes. The optimization between the minimization of the non-uniformity in the output powers and the minimization of power loss for the different inputs of a general N×N MMI coupler is formulated and used in the design of 4×4 and 8×8 MMI couplers.

Using FIMMPROP simulations diverse MMI couplers that are used in the different proposed IPPAS elements are designed including a -3dB 2×2 MMI coupler, crossover 2×2 MMI coupler, -6dB 4×4 MMI coupler, -3dB MMI coupler and -9dB 8×8 MMI coupler. All of the designed MMI couplers are compatible with each other; they all have the same pitch size separating the centers of their adjacent I/O ports. This compatibility in design have had made it possible to combine different size splitter/combiner MMI couplers to form variety of IPPAS elements. Additionally, the designed MMI couplers have typical parameters and small footprints. Taking the -3dB 2×2 MMI coupler as an example, it has a footprint of 4 μm × 60.66 μm with figures of merit of 0.053 dB of imbalance and 0.11 dB of excess loss based on simulation. Although these parameters belonging to the -3dB 2×2 MMI coupler seemed to be close to ideal, the imbalance and excess loss figures of merit become more significant for larger size MMI couplers. The designed -6dB 4×4 MMI coupler has a footprint of 8 μm × 122.2 μm with maximum imbalance of 0.074 dB and maximum excess loss of 0.377 dB based on simulation.

The analysis, design and simulation of the NEMS-operated phase shifters are the objectives of chapter (3). The currently designed phase shifter is capable of providing up to 180º of phase shift difference at the expense of about 1.1 dB of excess loss based on simulation. The phase shifter is composed of 15 cascaded under-etched slot waveguides separated by supporting slot waveguides that are not under-etched. High efficiency (97%) transition slot couplers are designed to couple the under-etched slotted waveguides and provide biasing voltage to one of the suspended slotted silicon beams of the phase shifter.

Testing the performance of the designed phase shifter is among the scheduled tasks in this research. Introducing a difference in the path length of the two branches interconnecting the splitter/combiner MMI couplers of the 2×2 IPPAS element introduces interferograms in the response of the outputs of this switch element. The shift in location of the peaks of these interferograms associated with the externally applied voltages facilitates the measure of the phase shift introduced by the investigated phase shifters. This kind of study has been conducted based on simulations and numerical analysis and will be utilized in the testing procedure. Examining the speed of the designed NEMS-operated phase shifter in lab is also planned. Reasoning the parameters that limit the possible speed of the designed active phase shifter should be looked at in the testing procedure.

Introducing differences in the path length of the branches interconnecting the splitter/combiner MMI couplers for the 4×4 and 8×8 IPPAS elements handle utilizing a verity of applications including WDM with active tuning capability for the re-localization of the passbands in the wavelength domain. The design of a 4×4 WDM-IPPAS element has been investigated and plans to fabricate and test it is undergoing.

REFERENCES

[1] K. Van Acoleyen, J. Roels, P. Mechet, T. Claes, D. Van Thourhout and R. Baets, “Ultracompact Phase Modulator Based on a Cascade of NEMS-Operated Slot Waveguides Fabricated in Silicon-on-Insulator,” IEEE Photonics Journal, Vol. 4, No. 3, pp. 778-788, June 2012.

[2] K. Voigt, L. Zimmermann, G. Winzer, H. Tian, B. Tillack and K. Petermann, “Fully Passive Si-Photonic 90° Hybrid for Coherent Receiver Applications,” ECOC Technical Digest, OSA, pp. 1-3, 2011.

[3] C. H. Lien, H. H. Lin, S. W. Weng, H. J. Wang and W. C. Chang, “A Compact Photonic Switch Based on Multimode Interference with Partial Index Modulation Regions,” Microwave and Optical Technology Letters, Vol. 33, No. 3, pp. 174-176, 2002.

[4] G. Singh, R. P. Yadav and V. Janyani, “Multimode Interference (MMI) Coupler Based All Optical Switch: Design, Applications and Performance Analysis,” International Journal of Recent Trends in Engineering, Vol. 1, No. 3, pp. 115-119, 2009.

[5] S. L. Tsao, H. C. Guo and Y. J. Chen, “Design of a 2 × 2 MMI MZI SOI Electro-optic Switch Covering C Band and L Band,” Microwave and Optical Technology Letters, Vol. 33, No. 4, pp. 262-265, 2002.

[6] X. Xue-Jun, C. Shao-Wu, X. Hai-Hua, S. Yang, Y. Yu-De, Y. Jin-Zhong and W. Qi-Ming, “High-Speed 2×2 Silicon-Based Electro-optic Switch with Nanosecond Switch Time,” Chinese Physics B, Vol. 18, No. 9, pp. 3900-3904, 2009.

[7] L. M. Augustin, R. Hanfoug, J. J. G. M. van der Tol, W. J. M. de Laat and M. K. Smit, “A Compact Integrated Polarization Splitter/Converter in InGaAsP-InP,” IEEE Photonics Technology Letters, Vol. 19, No. 17, pp. 1286-1288, 2007.

[8] T. T. Le and L. W. Cahill, “The Design of 4×4 Multimode Interference Coupler Based Microring Resonators on an SOI Platform,” Journal of Telecommunications and Information Technology, pp. 58-62, 2009.

[9] S. H. Jeong and K. Morito, “Compact and Wideband Optical 90º Hybrid Based on a One-Way Tapered MMI Coupler,” OSA/OFC/NFOEC, 2011.

[10] K. Voigt, L. Zimmermann, G. Winzer, K. Petermann and C. M. Weinert, “Silicon-on-Insulator 90° Optical Hybrid Using 4×4 Waveguide Couplers with C-Band Operation,” ECOC, pp. 99-100, 2008.

[11] L. Zimmermann, K. Voigt, G. Winzer, K. Petermann and C. M. Weinert, “C-band optical 90°-Hybrids Based on Silicon-on-Insulator 4×4 Waveguide Couplers,” IEEE Photonics Technology Letters, Vol. 21, No. 3, pp. 143-145, 2009.

[12] S. Abdul-Majid, I. I. Hasan, P. J. Bock and T. J. Hall, “Design, Simulation and Fabrication of a 90° SOI Optical Hybrid Based on the Self-Imaging Principle,” Proc. of SPIE, Vol. 7719, 77190E, pp. 1-9, 2010.

[13] M. R. Paiam and R. I. MacDonald, “Design of Phased-Array Wavelength Division Multiplexers Using Multimode Interference Couplers,” Applied Optics, Vol. 36, No. 21, pp. 5097-5108, 1997.

[14] C. Yuan-Yuan, Y. Di, Y. Jin-zhong, S. Mei and X. Su-Xia, “Design of an Ultra-Compact 3 dB MMI Coupler,” Optoelectronics Letters, Vol. 5, No. 6, pp. 427-429, 2009.

[15] D. S. Levy, R. Scarmozzino, Y. M. Li and R. M. Osgood, “A New Design for Ultracompact Multimode Interference-Based 2×2 Couplers,” IEEE Photonics Technology Letters, Vol. 10, No. 1, pp. 96-98, 1998.

[16] Hill, M. T., Leijtens, X. J. M., Khoe, G. D. and Smit, M. K., “Optimizing Imbalance and Loss in 2×2 3-dB Multimode Interference Couplers Via Access Waveguide Width,” Journal of Lightwave Technology, Vol. 21, No. 10, pp. 2305-2313, 2003.

[17] Katsunari Okamoto, Fundamentals of Optical Waveguides, 2’nd Edition, Elsevier Inc., 2006.

[18] Joseph W. Goodman, Introduction to Fourier Optics, 3’rd Edition, Roberts and Company Publishers, 2005.

[19] M. Bachmann, P. A. Besse and H. Melchior, “General Self-Imaging Properties in N×N Multimode Interference Couplers Including Phase Relations,” Applied Optics, Vol. 33, No. 18, pp. 3905-3911, 1994.

[20] L. B. Soldano and E. C. M. Pennings, “Optical Multimode Interference Devices Based on Self-Imaging: Principles and Applications,” Journal of Lightwave Technology, Vol. 13, No. 4, pp. 615-627, 1995.

[21] Ching-Ting Lee, Mount-Learn Wu, Lih-Gen Sheu, Ping-Lin Fan and Jui-Ming Hsu, “Design and Analysis of Completely Adiabatic Tapered Waveguides by Conformal Mapping,” Journal of Lightwave Technology, Vol. 15, No. 2, pp. 403-410, 1997.

[22] Bert Luyssaert, Peter Bienstman, Peter Vandersteegen, Pieter Dumon and Roel Baets, “Efficient Nonadiabatic Planar Waveguide Tapers,” Journal of Lightwave Technology, Vol. 23, No. 8, pp. 2462-2468, 2005.

[23] Daoxin Dai, Yongbo Tang and John E Bowers, “Mode conversion in tapered submicron silicon ridge optical waveguides,” Optical Society of America, pp. 13425-13439, 2012.

[24] Van Acoleyen, K., Roels, J., Claes, T., Van Thourhout, D. and Baets, R., “NEMS-based optical phase modulator fabricated on silicon-on-insulator,” Proc. 8th Int. Conference GFP, London, U.K., 371-373 (2011).